









A two-fluid solar-wind model with intermittent Alfvénic turbulence

Benjamin Divakar Giles Chandran¹ , Toby Adkins^{2,3} , Stuart D. Bale⁴,
Vincent David¹ , Jasper Halekas⁵, Kristopher Klein⁶ , Romain Meyrand¹ ,
Jean C. Perez⁷ , Munehito Shoda⁸, Jonathan Squire³  and
Evan Lowell Yerger¹ 

¹Space Science Center and Department of Physics and Astronomy, University of New Hampshire,
Durham, NH 03824, USA

²Princeton Plasma Physics Laboratory, Princeton, NJ 08540, USA

³Department of Physics, University of Otago, Dunedin, New Zealand

⁴Space Sciences Laboratory and Department of Physics, University of California, Berkeley, CA 94720,
USA

⁵Department of Physics & Astronomy, University of Iowa, Iowa City, IA 52242, USA

⁶Lunar and Planetary Laboratory, University of Arizona, Tucson, AZ 85721-0092, USA

⁷Department of Aerospace, Physics and Space Sciences, Florida Institute of Technology, Melbourne, FL
32901, USA

⁸Department of Earth and Planetary Science, University of Tokyo, Tokyo, Japan

Corresponding author: Benjamin Divakar Giles Chandran, benjamin.chandran@unh.edu

(Received 2 February 2025; revision received 16 June 2025; accepted 17 June 2025)

In one of the leading theories for the origin of the solar wind, photospheric motions launch Alfvén waves (AWs) that propagate along open magnetic-field lines through the solar atmosphere and into the solar wind. The radial variation in the Alfvén speed causes some of the AWs to reflect, and counter-propagating AWs subsequently interact to produce Alfvénic turbulence, in which AW energy cascades from long wavelengths to short wavelengths and dissipates, heating the plasma. In this paper we develop a one-dimensional two-fluid solar-wind model that includes Alfvénic turbulence, proton temperature anisotropy and a novel method for apportioning the turbulent heating rate between parallel proton heating, perpendicular proton heating and electron heating. We employ a turbulence model that accounts for recent observations from NASA’s Parker Solar Probe, which find that AW fluctuations in the near-Sun solar wind are intermittent and less anisotropic than in previous models of anisotropic magnetohydrodynamic turbulence. Our solar-wind model reproduces a wide range of remote observations of the corona and *in-situ* measurements of the solar wind, and our turbulent heating model consists of analytic equations that could be usefully incorporated into other solar-wind models and numerical models of more distant astrophysical plasmas.

Key words: astrophysical plasmas, space plasma physics, plasma nonlinear phenomena

1. Introduction

Heating causes the Sun's outer corona to become gravitationally unbound and expand, forming the solar wind, whose structure has been characterised in detail by numerous *in-situ* measurements over the past six decades (Verscharen *et al.* 2019; Raouafi *et al.* 2023). The distribution of solar-wind speeds measured far from the Sun is bimodal, with one peak in the distribution at speeds in the range of 300–500 km s^{−1} (slow solar wind) and another peak in the range of 700–800 km s^{−1} (fast solar wind) (see, e.g. Neugebauer & Snyder 1966; Gosling *et al.* 1976). Near solar minimum (the period of the solar cycle in which there are the fewest sunspots), most of the heliosphere is filled with fast solar wind that emanates from the Sun's polar coronal holes,¹ and slow solar wind is concentrated at low heliolatitudes, near the ecliptic (the plane of Earth's orbit) (Goldstein *et al.* 1996; McComas *et al.* 2000). Near solar maximum, the solar wind is much more disordered, and fast wind and slow wind can be found at virtually all heliolatitudes (McComas *et al.* 2003).

Early work on the solar wind's origin found that fast solar wind could only arise in the presence of significant extended heating out to heliocentric distances r of tens of solar radii, leading Eugene Parker to conjecture that the corona and solar wind are heated by the dissipation of waves (Parker 1965, p. 686). The experimental detection of turbulence in the interplanetary medium led to a modification of this conjecture, that the solar wind is heated by turbulence (Coleman 1968). Shortly thereafter, Belcher & Davis (1971) analysed *in-situ* measurements from the Mariner 5 spacecraft and showed that the solar wind is permeated by broad-band, Alfvén-wave (AW)-like fluctuations that propagate away from the Sun in the plasma frame. Their work provided substantial early support for the idea that the solar wind is strongly heated by Alfvénic turbulence, by which we mean fluctuations in the velocity and magnetic field, $\delta\mathbf{v}$ and $\delta\mathbf{B}$, that have comparable energies and are only weakly compressive, meaning that the fractional density fluctuations $\delta n/n_0$ and magnetic-field-strength fluctuations $\delta B/B_0$ are small compared with $|\delta\mathbf{B}|/B_0$. This type of turbulence can be viewed as the nonlinear development of interacting AWs.

More recently, remote observations from the Solar Optical Telescope on the Hinode spacecraft (De Pontieu *et al.* 2007) and *in-situ* measurements from the Parker Solar Probe (PSP) and Solar Orbiter (Halekas *et al.* 2023; Rivera *et al.* 2024) have shown that volume-filling AW-like fluctuations carry sufficient energy to power the fast solar wind. These observations have helped to solidify Alfvénic turbulence as the leading candidate to explain the majority of the energisation of the fast solar wind. Alfvénic turbulence may also be an important energetic driver of slow solar wind that emerges from small coronal holes or the boundaries of large coronal holes (e.g. Cranmer, van Ballegoijen & Edgar 2007; Chen *et al.* 2020; Chandran 2021), as well as the heating of regions of the solar corona with closed magnetic-field lines (Rappazzo *et al.* 2007, 2017; Downs *et al.* 2016; Mikić *et al.* 2018; Boe *et al.* 2021, 2022).

The generation of the solar wind by Alfvénic turbulence has been explored in detail in a number of numerical solar-wind models (e.g. Suzuki & Inutsuka 2005;

¹Coronal holes are regions of the corona with open magnetic-field lines that connect the coronal base to the distant heliosphere.

Suzuki 2006; Cranmer *et al.* 2007; Verdini *et al.* 2010; van der Holst *et al.* 2014; Lionello *et al.* 2014*a, b*; Usmanov, Goldstein & Matthaeus 2014; Shoda *et al.* 2019; Réville *et al.* 2020). An important ingredient in these models is the reflection of AWs that arises because the Alfvén speed v_A varies with r (Heinemann & Olbert 1980; Velli 1993). The Sun launches only outward-propagating waves, but reflection leads to a mixture of counter-propagating AWs at all r .² Counter-propagating AWs interact nonlinearly to produce Alfvénic turbulence, causing fluctuation energy to cascade from large scales (wavelengths) to small scales (Kraichnan 1965). Although AWs are virtually undamped at the large wavelengths that characterise the bulk of the AW energy launched by the Sun, the fluctuation energy in Alfvénic turbulence dissipates rapidly after it cascades to sufficiently small scales. The rate of plasma heating by turbulence thus becomes insensitive to the linear damping rate of large-scale AWs and is determined instead by the rate at which AW energy cascades from large scales to small scales. This energy-cascade rate is, in turn, influenced by the rate of AW reflection, which is proportional to the Alfvén-speed gradient.

Although there is broad agreement that Alfvénic turbulence is energetically important in the corona and solar wind, the way that such turbulence heats the plasma is not well understood. A long-standing puzzle concerns the way that the turbulent heating power is partitioned between particle species and between parallel and perpendicular heating (see, e.g. Quataert 1998; Leamon *et al.* 1998; Howes 2024), where perpendicular (parallel) heating increases the speed of thermal motions perpendicular (parallel) to the magnetic field. The Ultraviolet Coronagraph Spectrometer (UVCS) and Solar Ultraviolet Measurements of Emitted Radiation (SUMER) instruments on the Solar and Heliospheric Observatory have provided important constraints on this partitioning. In particular, UVCS and SUMER measurements show that $T_{\perp p} > T_{\parallel p}$, $T_{\perp p} > T_e$ and $T_{\perp O^{+5}} \gg T_{\perp p}$ in coronal holes, where $T_{\perp p}$ and $T_{\parallel p}$ are the perpendicular and parallel proton temperatures, T_e is the electron temperature and $T_{O^{+5}}$ is the temperature of O^{+5} ions (Kohl *et al.* 1998; Landi 2008). These inequalities suggest that ion cyclotron heating plays a dominant role in dissipating the turbulence (e.g. Hollweg & Isenberg 2002). However, in theoretical models and numerical simulations, the fluctuation energy in Alfvénic turbulence cascades anisotropically, resulting in small-scale fluctuations that are elongated along the magnetic field \mathbf{B} (Shebalin, Matthaeus & Montgomery 1983; Goldreich & Sridhar 1995; Cho & Vishniac 2000; Mallet, Schekochihin & Chandran 2015). Such fluctuations have smaller wavenumber components k_{\parallel} in the \mathbf{B} direction than would be expected in isotropic turbulence. As the AW frequency is $k_{\parallel} v_A$, this reduction in k_{\parallel} reduces the frequencies of the small-scale fluctuations, preventing them from reaching the ion cyclotron frequency (e.g. Cranmer & van Ballegoijen 2003). Explaining the observed perpendicular ion temperatures thus remains an important challenge for solar-wind models based on Alfvénic turbulence.

More generally, it remains challenging to predict the time-dependent structure of the three-dimensional (3-D) solar wind and solar corona using numerical models of any kind. The premise of this paper is that an improved, physics-based description of turbulent heating will increase the accuracy of 3-D solar-wind models, which in turn will contribute to our ability to model and predict space weather. With this long-term goal in mind, we aim to show how recent advances in modelling solar-wind turbulence can be incorporated into a one-dimensional (1-D) solar-wind model

²Parametric decay also generates inward-propagating AWs, but we do not consider this process in this paper.

and to test this 1-D model using a wide range of solar-wind observations. We note that our method for describing turbulence and turbulent heating is based on analytic expressions that could be included straightforwardly in 3-D models.

The remainder of this paper is organised as follows. We present the main equations of our model in § 2 and the details of our turbulent heating model in § 3. In § 4 we present numerical examples based on the axisymmetric solar-minimum magnetic-field model of Banaszkiewicz, Axford & McKenzie (1998) and Hackenberg, Marsch & Mann (2000) and compare our model with observations. We summarise our findings and conclude in § 5.

2. The principal equations of the model

Our model is very similar to the two-fluid solar-wind model with proton temperature anisotropy that was developed by Chandran *et al.* (2011), but we use a different prescription for the turbulent heating rate (§ 3) and include radiative cooling. We describe our approach in detail in the following subsections.

2.1. Magnetic geometry and numerical domain

We limit our model to heliocentric distances less than³

$$r_{\max} = 72R_{\odot}. \quad (2.1)$$

This enables us to neglect the effects of solar rotation on the direction of the background magnetic field \mathbf{B} and to treat \mathbf{B} as approximately radial. We then analyse the solar-wind outflow within a narrow magnetic flux tube centred on a radial magnetic-field line. We take the solar-wind outflow velocity \mathbf{U} to be everywhere parallel to the magnetic field \mathbf{B} , setting

$$\mathbf{U} = U\hat{\mathbf{b}}, \quad (2.2)$$

where $\hat{\mathbf{b}} = \mathbf{B}/B$. The magnetic-field-strength profile $B(r)$ is arbitrary, but fixed in time. Although we allow the magnetic field to undergo super-radial expansion (Kopp & Holzer 1976), the radially oriented magnetic flux tube that we consider is sufficiently narrow that we may approximate

$$\mathbf{B} \cdot \nabla \rightarrow B \frac{\partial}{\partial r}. \quad (2.3)$$

The cross-sectional area of the flow $a(r)$ is related to $B(r)$ by magnetic flux conservation,

$$\frac{a(r)}{a(r_b)} = \frac{B(r_b)}{B(r)}, \quad (2.4)$$

where r_b is the minimum heliocentric distance in the model, which we take to lie somewhere in the upper transition region, just beneath the corona.

³Although we solve the equations of our model only at $r \leq r_{\max}$, energy conservation allows us to predict the asymptotic solar-wind outflow velocity U_{∞} of a solar-wind stream at $r \gg r_{\max}$ based on the properties of the solar-wind stream at $r \leq r_{\max}$, as we discuss further in § 4.3, where we compare our model with measurements from the Ulysses spacecraft.

2.2. Moments of the Vlasov equation

Following a number of authors (e.g. Kulsrud 1983; Snyder, Hammett & Dorland 1997; Sharma *et al.* 2006), we take moments of the Vlasov equation for a proton–electron plasma in the limit in which the plasma frequency and cyclotron frequency are much larger than any other frequency of interest. In this limit, the plasma is quasi-neutral, and the proton and electron distribution functions are gyrotropic. We view all moments of these distribution functions (e.g. the proton density n , which equals the electron density) as the sum of a background value and a fluctuation, where the background value of a quantity is its average over the cross-section of the flux tube at fixed r . The background values are thus functions of r and t alone.

The resulting equations allow for proton temperature anisotropy, but we assume an isotropic electron temperature T_e and determine the radial component of the electron heat flux q_e using a simple closure (§ 2.4). In contrast, $q_{\perp p}$ and $q_{\parallel p}$, the radial components of the perpendicular and parallel proton heat fluxes, respectively, evolve dynamically in a way that depends upon three different types of fourth velocity moments of the proton distribution function. To close the proton fluid equations, we take these fourth velocity moments to have the same values that they would have in a bi-Maxwellian plasma with the same $T_{\perp p}$ and $T_{\parallel p}$ as the actual plasma. We incorporate reflection-driven AW turbulence by treating the dominant, outward-propagating AWs as a separate fluid with energy density \mathcal{E}_w that interacts with the plasma via a wave-pressure force and turbulent heating.

The eight dependent variables in our model (n , U , T_e , $T_{\perp p}$, $T_{\parallel p}$, $q_{\perp p}$, $q_{\parallel p}$ and \mathcal{E}_w) satisfy the following eight equations (Chandran *et al.* 2011):

$$\frac{dn}{dt} = -\frac{n}{a} \frac{\partial}{\partial r} (aU), \quad (2.5)$$

$$\frac{dU}{dt} = -\frac{k_B}{\rho} \frac{\partial}{\partial r} [n(T_e + T_{\parallel p})] + \frac{k_B(T_{\perp p} - T_{\parallel p})}{m_p a} \frac{\partial a}{\partial r} - \frac{GM_\odot}{r^2} - \frac{1}{2\rho} \frac{\partial \mathcal{E}_w}{\partial r}, \quad (2.6)$$

$$\frac{3}{2} n^{5/3} k_B \frac{d}{dt} \left(\frac{T_e}{n^{2/3}} \right) = Q_e - \frac{1}{a} \frac{\partial}{\partial r} (aq_e) + 3\nu_{pe} n k_B (T_p - T_e) - n^2 \Lambda_{\text{rad}}(T_e), \quad (2.7)$$

$$\begin{aligned} B n k_B \frac{d}{dt} \left(\frac{T_{\perp p}}{B} \right) &= Q_{\perp p} - \frac{1}{a^2} \frac{\partial}{\partial r} (a^2 q_{\perp p}) \\ &+ \frac{1}{3} \nu_p n k_B (T_{\parallel p} - T_{\perp p}) + 2\nu_{pe} n k_B (T_e - T_{\perp p}), \end{aligned} \quad (2.8)$$

$$\begin{aligned} \frac{n^3 k_B}{2B^2} \frac{d}{dt} \left(\frac{B^2 T_{\parallel p}}{n^2} \right) &= Q_{\parallel p} - \frac{1}{a} \frac{\partial}{\partial r} (a q_{\parallel p}) \\ &+ \frac{q_{\perp p}}{a} \frac{\partial a}{\partial r} + \frac{1}{3} \nu_p n k_B (T_{\perp p} - T_{\parallel p}) + \nu_{pe} n k_B (T_e - T_{\parallel p}), \end{aligned} \quad (2.9)$$

$$n^2 \frac{d}{dt} \left(\frac{q_{\perp p}}{n^2} \right) = -\frac{n k_B^2 T_{\parallel p}}{m_p} \frac{\partial T_{\perp p}}{\partial r} + \frac{n k_B^2 T_{\perp p} (T_{\perp p} - T_{\parallel p})}{m_p a} \frac{\partial a}{\partial r} - \nu_p q_{\perp p}, \quad (2.10)$$

$$\frac{n^4}{B^3} \frac{d}{dt} \left(\frac{B^3 q_{\parallel p}}{n^4} \right) = -\frac{3n k_B^2 T_{\parallel p}}{2m_p} \frac{\partial T_{\parallel p}}{\partial r} - \nu_p q_{\parallel p} \quad (2.11)$$

and (Dewar 1970)

$$\frac{\partial \mathcal{E}_w}{\partial t} + \frac{1}{a} \frac{\partial}{\partial r} [a(U + v_A) \mathcal{E}_w] + \frac{\mathcal{E}_w}{2a} \frac{\partial}{\partial r} (aU) = -Q. \quad (2.12)$$

Here $v_A = B/\sqrt{4\pi\rho}$, $\rho = m_p n$ is the mass density, M_\odot is the mass of the Sun and

$$\frac{d}{dt} = \frac{\partial}{\partial t} + U \frac{\partial}{\partial r} \quad (2.13)$$

is the time derivative in the plasma frame. The quantities Q_e , $Q_{\perp p}$ and $Q_{\parallel p}$ are, respectively, the electron heating rate, the perpendicular proton heating rate and the parallel proton heating rate resulting from the dissipation of AW turbulence (see §3), and

$$Q = Q_e + Q_{\perp p} + Q_{\parallel p} \quad (2.14)$$

is the total turbulent heating rate. The quantity

$$\nu_{pe} = \frac{4\sqrt{2\pi m_e} e^4 n \ln \Lambda}{3m_p (k_B T_e)^{3/2}} \quad (2.15)$$

is the Coulomb collision frequency for the exchange of energy between protons and electrons (Schunk 1975), where m_p and m_e are the proton and electron masses, respectively, and $\ln \Lambda$ is the Coulomb logarithm, which we set equal to 23. The proton–proton collision frequency in our model is given by

$$\nu_p = \nu_{pp,C} + \nu_{inst}, \quad (2.16)$$

where

$$\nu_{pp,C} = \frac{4\sqrt{\pi} e^4 n \ln \Lambda}{3\sqrt{m_p} (k_B T_p)^{3/2}} \quad (2.17)$$

is the proton–proton Coulomb collision frequency (Schunk 1975),

$$T_p = \frac{2T_{\perp p} + T_{\parallel p}}{3}, \quad (2.18)$$

and ν_{inst} is a model temperature-isotropisation rate resulting from small-scale plasma fluctuations that grow when the proton temperature anisotropy exceeds the threshold of the oblique firehose or mirror instability (see §2.5).

The quantity $\Lambda_{rad}(T_e)$ on the right-hand side of (2.7) is the optically thin radiative loss function, which we take to have the same value as the quantity $\Lambda(T)$ in the single-fluid model of Cranmer *et al.* (2007). To determine this latter function, we read off the value of $\Lambda(T)$ from figure 1 of Cranmer *et al.* (2007) at 35 evenly spaced values of $\log_{10}[T/(1 \text{ K})]$ ranging from 3.6 to 7.0. We then approximate $\log_{10} \Lambda(T)$ as a continuous and piecewise linear function of $\log_{10} T$ that passes through these 35 ordered pairs of $(T, \Lambda(T))$ values. We plot the resulting value of $\Lambda_{rad}(T_e)$ in figure 1.

2.3. Total energy equation

Multiplying (2.6) by ρU and adding the resulting equation to the sum of (2.7)–(2.9) and (2.12) yields

$$\frac{\partial \mathcal{E}_{tot}}{\partial t} + \frac{1}{a} \frac{\partial}{\partial r} (a F_{tot}) = -n^2 \Lambda_{rad}(T_e), \quad (2.19)$$

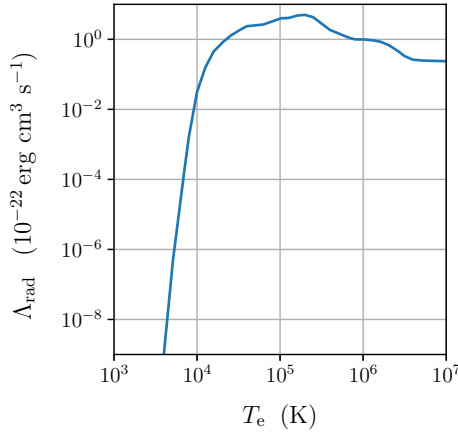


FIGURE 1. The optically thin radiative loss function appearing in (2.7) and (2.19).

where

$$\mathcal{E}_{\text{tot}} = \frac{\rho U^2}{2} - \frac{GM_{\odot}\rho}{r} + nk_B \left(\frac{3T_e}{2} + T_{\perp p} + \frac{T_{\parallel p}}{2} \right) + \mathcal{E}_w \quad (2.20)$$

is the total energy density and

$$F_{\text{tot}} = \frac{\rho U^3}{2} - \frac{UGM_{\odot}\rho}{r} + Unk_B \left(\frac{5T_e}{2} + T_{\perp p} + \frac{3T_{\parallel p}}{2} \right) + q_e + q_{\perp p} + q_{\parallel p} + \left(\frac{3U}{2} + v_A \right) \mathcal{E}_w \quad (2.21)$$

is the total energy flux. In steady state, and at heights $\gtrsim 0.1 R_{\odot}$ above the photosphere where radiative cooling is negligible, aF_{tot} becomes independent of r .

2.4. Electron heat flux

In the low corona, the Coulomb mean free path is much smaller than the temperature scale height, and the radial component of the electron heat flux is well approximated by the Spitzer formula (Spitzer & Härm 1953)

$$q_{e,s} = -\alpha_s T_e^{5/2} \frac{\partial T_e}{\partial r}, \quad (2.22)$$

where

$$\alpha_s = \frac{1.84 \times 10^{-5}}{\ln \Lambda} \text{ erg s}^{-1} \text{ K}^{-7/2} \text{ cm}^{-1}. \quad (2.23)$$

We approximate the radial component of the electron heat flux far outside the corona using Hollweg's collisionless heat-flux formula (Hollweg 1974, 1976)

$$q_{e,H} = \frac{3}{2} \alpha_H Unk_B T_e, \quad (2.24)$$

where α_H is a dimensionless constant that we treat as a free parameter. To obtain a continuous transition between these two heat-flux regimes, we set

$$q_e = \frac{(r/r_H)^4 q_{e,H}}{1 + (r/r_H)^4} + \frac{q_{e,s}}{1 + (r/r_H)^4}, \quad (2.25)$$

where r_H is a free parameter.

2.5. Temperature isotropisation from firehose and mirror instabilities

The proton temperature-anisotropy ratio $R = T_{\perp p}/T_{\parallel p}$ in the solar wind is observed to be limited from above by the mirror instability threshold

$$R_m = 1 + 0.77(\beta_{\parallel p} + 0.016)^{-0.76} \quad (2.26)$$

and from below by the oblique firehose instability threshold

$$R_f = 1 - 1.4(\beta_{\parallel p} + 0.11)^{-1} \quad (2.27)$$

(Kasper, Lazarus & Gary 2002; Hellinger *et al.* 2006; Bale *et al.* 2009),⁴ where

$$\beta_{\parallel p} = \frac{8\pi n k_B T_{\parallel p}}{B^2}. \quad (2.28)$$

This suggests that when the plasma crosses one of these thresholds, short-wavelength fluctuations grow and cause pitch-angle scattering that drives the plasma back into the stable region of parameter space. We incorporate such instability-induced pitch-angle scattering into our model through the term ν_{inst} in (2.16), where

$$\nu_{\text{inst}} = \nu_0 \exp \left[\frac{12(R - R_m)}{R_m} \right] + \nu_0 \exp \left[\frac{12(\bar{R}_f - R)}{\bar{R}_f} \right], \quad (2.29)$$

$\nu_0 = 0.02\sqrt{GM_{\odot}/R_{\odot}^3}$ and $\bar{R}_f = \max(R_f, 10^{-6})$ (cf. Sharma *et al.* 2006; Chandran *et al.* 2011).

3. Alfvénic turbulence and turbulent heating

In this section we present our model of reflection-driven Alfvénic turbulence and turbulent heating. We describe how we determine the radial profiles of the fluctuation amplitudes, correlation lengths and energy-cascade rate in §§ 3.1 and 3.2. Sections 3.3 and 3.4 describe how we model the scale dependence of the fluctuation amplitudes within the inertial range. The inertial range is the range of scales that is smaller than the outer scale but larger than the dissipation scale, below which dissipation becomes important. We take the dissipation scale (measured perpendicular to the magnetic field) to be the proton gyroradius

$$\rho_p = \frac{v_{\perp th, p}}{\Omega_p}, \quad (3.1)$$

where $v_{\perp th, p} = (2k_B T_{\perp p}/m_p)^{1/2}$ is the proton perpendicular thermal speed. In some cases, a finite interval of scales at the large-scale end of the inertial range is in the weak-turbulence regime. Section 3.3 describes how we model such weakly turbulent fluctuations when they arise. In general, for coronal holes and the near-Sun solar wind, the majority of the inertial range is in the strong-turbulence regime, and § 3.4 describes how we model strong reflection-driven Alfvénic turbulence. We then discuss how we model dissipation and turbulent heating in § 3.5.

⁴Equations (2.26) and (2.27) are the values of R at which the linear growth rates for the instabilities in a bi-Maxwellian plasma are $10^{-3}\Omega_p$, where Ω_p is the proton cyclotron frequency (Hellinger *et al.* 2006).

3.1. The root-mean-square amplitudes of the turbulent fluctuations

We describe the turbulent fluctuations using the Elsasser variables (Elsasser 1950)

$$\delta \mathbf{z}^{\pm} = \delta \mathbf{v} \pm \frac{\delta \mathbf{B}}{\sqrt{4\pi m_p n}}. \quad (3.2)$$

We take the background magnetic field \mathbf{B} to point toward the Sun, and therefore, $\delta \mathbf{z}^+$ ($\delta \mathbf{z}^-$) represents Alfvénic fluctuations propagating away from (toward) the Sun in the plasma frame. We define the perpendicular and parallel outer scales $L_{\perp}(r)$ and $L_{\parallel}(r)$ to be the length scales that make the dominant contribution to the fluctuation energy.⁵ Although L_{\perp} can be different (and evolve with r differently) for $\delta \mathbf{z}^+$ and $\delta \mathbf{z}^-$ (Meyrand *et al.* 2025), for simplicity, we take it to be the same.

The energy density of outward-propagating AWs is $\mathcal{E}_w = m_p n (\delta z_{\text{rms}}^+)^2 / 4$, where $\delta z_{\text{rms}}^{\pm}$ is the root-mean-square (r.m.s.) amplitude of $\delta \mathbf{z}^{\pm}$. Equivalently,

$$\delta z_{\text{rms}}^+ = 2 \left(\frac{\mathcal{E}_w}{m_p n} \right)^{1/2}. \quad (3.3)$$

At $r \lesssim 20 R_{\odot}$, where most of the heating and acceleration of the solar wind take place, the turbulence is highly imbalanced (e.g. Verdini & Velli 2007; Perez & Chandran 2013; Chen *et al.* 2020; McIntyre *et al.* 2024), meaning that

$$\delta z_{\text{rms}}^- \ll \delta z_{\text{rms}}^+. \quad (3.4)$$

We derive our turbulent heating model in this highly imbalanced limit. Equations (3.2) and (3.4) imply that the r.m.s. fluctuating velocity is approximately

$$\delta v_{\text{rms}} = \frac{1}{2} \delta z_{\text{rms}}^+. \quad (3.5)$$

We estimate δz_{rms}^- by balancing the rate at which $\delta \mathbf{z}^-$ is produced by reflection against the rate at which $\delta \mathbf{z}^-$ cascades and dissipates, which yields

$$\delta z_{\text{rms}}^- = \frac{L_{\perp}(U + v_A)}{v_A} \left| \frac{\partial v_A}{\partial r} \right|. \quad (3.6)$$

Equation (3.6) was originally derived in the strong-turbulence regime by Dmitruk *et al.* (2002) for the case without background flow and by Chandran & Hollweg (2009) for the case with background flow. Subsequently, Chandran & Perez (2019) showed that (3.6) is also approximately valid when $\delta \mathbf{z}^-$ fluctuations are in the weak-turbulence regime. We discuss the weak- and strong-turbulence regimes further in § 3.3 and 3.4

In the numerical examples that we present in § 4, v_A varies so rapidly near $r = r_b$ (the minimum heliocentric distance in the model, approximately 2000 km above the photosphere) that the value of δz_{rms}^- in (3.6) can exceed δz_{rms}^+ , violating the assumptions under which (3.6) was derived. To avoid this, we replace $|\partial v_A / \partial r|$ in (3.6) with

$$\left| \frac{\partial v_A}{\partial r} \right|_{\text{eff}} = \min \left(\left| \frac{\partial v_A}{\partial r} \right|_{\text{eff}}, \frac{c_{\text{refl}} \delta z_{\text{rms}}^+}{L_{\perp}} \right), \quad (3.7)$$

⁵Often in the solar wind the magnetic power spectrum is $\propto 1/f$ at small frequencies f (but see Davis *et al.* 2023; Huang *et al.* 2023). For such cases, we identify the outer scale with the break between the $1/f$ range and the inertial range.

where the constant c_{refl} is an adjustable free parameter. Equation (3.7), in combination with (3.6), prevents $\delta z_{\text{rms}}^-/\delta z_{\text{rms}}^+$ from exceeding $c_{\text{refl}}(U + v_A)/v_A$.

For simplicity, we make the approximation that L_{\perp}^{-1} and $(L_{\parallel}^+)^{-1}$ scale with radius in the same way as the perpendicular and parallel wavenumbers of outward-propagating AWs in the WKB (Wentzel–Kramers–Brillouin) approximation in a steady-state solar wind with a radial magnetic field. This yields

$$L_{\perp}(r) = L_{\perp kG} \left[\frac{1 \text{ kG}}{B(r)} \right]^{1/2} \quad L_{\parallel}^+(r, t) = [U(r, t) + v_A(r, t)] \tau_b, \quad (3.8)$$

where $L_{\perp kG}$ is a free parameter and

$$\tau_b = \frac{L_{\perp}(r_b)}{\delta v_{\text{rms}}(r_b)} \quad (3.9)$$

is the approximate correlation time of the fluctuations at $r = r_b$.

3.2. The energy cascade in magnetohydrodynamics

We view the fluctuations as a collection of δz^{\pm} wave packets with length scales λ and l_{λ}^{\pm} measured perpendicular and parallel to the magnetic field, respectively, and amplitudes δz_{λ}^{\pm} . We take outer-scale wave packets to satisfy the equations

$$\delta z_{L_{\perp}}^{\pm} = \delta z_{\text{rms}}^{\pm}, \quad l_{L_{\perp}}^{\pm} = L_{\parallel}^{\pm}. \quad (3.10)$$

Each δz^{\pm} wave packet propagates at velocity $\mp v_A \hat{\mathbf{b}}$ while being distorted by nonlinear interactions with counter-propagating wave packets. As pointed out by Lithwick, Goldreich & Sridhar (2007), it is useful to consider the evolution of a ‘slice’ of a δz^{\pm} wave packet at perpendicular scale λ , that is, a cross-section of the δz^{\pm} wave packet in the plane perpendicular to \mathbf{B} . The time required for this slice to propagate through a counter-propagating δz^{\mp} wave packet of perpendicular scale λ is approximately

$$\tau_{\text{lin}, \lambda}^{\pm} = \frac{l_{\lambda}^{\mp}}{v_A}. \quad (3.11)$$

The time scale associated with the shearing of the δz^{\pm} wave packet by a δz^{\mp} wave packet at scale λ is

$$\tau_{\text{nl}, \lambda}^{\pm} = \frac{\lambda}{\delta z_{\lambda}^{\mp}}. \quad (3.12)$$

The critical-balance parameter is (Goldreich & Sridhar 1995)

$$\chi_{\lambda}^{\pm} = \frac{\tau_{\text{lin}, \lambda}^{\mp}}{\tau_{\text{nl}, \lambda}^{\mp}} = \frac{\delta z_{\lambda}^{\pm} l_{\lambda}^{\pm}}{\lambda v_A}, \quad (3.13)$$

where we have adopted the \pm labelling convention of Lithwick *et al.* (2007) (hereafter LGS07) for χ_{λ}^{\pm} . When $\chi_{\lambda}^+ \gtrsim 1$, a δz^- wave packet at scale λ is strongly sheared and distorted before it can propagate through a δz^+ wave packet at scale λ . In this strong-turbulence regime, the time required for a δz^- wave packet at perpendicular scale λ to pass its energy on to smaller scales is approximately

$$\tau_{\text{casc}, \lambda}^- = \frac{\lambda}{\delta z_{\lambda}^+} \quad (\text{if } \chi_{\lambda}^+ \geq 1). \quad (3.14)$$

On the other hand, when $\chi_\lambda^+ \ll 1$, each slice of a δz^- wave packet at scale λ passes through a counter-propagating δz^+ wave packet at scale λ before the slice is strongly distorted. In this weak-turbulence regime, the effects on the δz^- wave packet of consecutive ‘collisions’ with δz^+ wave packets at scale λ add incoherently, like the steps in a random walk. A δz^- wave packet undergoes a fractional distortion $\simeq \chi_\lambda^+$ during a single collision and is thus strongly distorted after $\sim (\chi_\lambda^+)^{-2}$ collisions. As the duration of a single collision is $\sim l_\lambda^+ / v_A$, the energy of a δz^- wave packet at scale λ cascades to smaller scales on the time scale (Kraichnan 1965; Ng & Bhattacharjee 1996, 1997; Goldreich & Sridhar 1997)

$$\tau_{\text{casc},\lambda}^- = (\chi_\lambda^+)^{-2} \frac{l_\lambda^+}{v_A} = (\chi_\lambda^+)^{-1} \frac{\lambda}{\delta z_\lambda^+} \quad (\text{if } \chi_\lambda^+ < 1). \quad (3.15)$$

The rate at which δz^\pm energy cascades to smaller scales at scale λ is

$$\epsilon_\lambda^\pm = \frac{m_p n (\delta z_\lambda^\pm)^2}{4\tau_{\text{casc},\lambda}^\pm}. \quad (3.16)$$

We take ϵ_λ^\pm to be independent of λ for $\rho_p \lesssim \lambda \leq L_\perp$, and we use the abbreviated notation ϵ^\pm to denote the value of ϵ_λ^\pm anywhere in this scale range. Applying (3.10) and (3.14) through (3.16) to the outer-scale δz^- fluctuations, we find that

$$\epsilon^- = \frac{m_p n (\delta z_{\text{rms}}^-)^2 \delta z_{\text{rms}}^+}{4L_\perp} \times \min(\chi_{L_\perp}^+, 1). \quad (3.17)$$

Equations (3.6), (3.13) and (3.17) imply that $\epsilon^- \propto L_\perp$ when $\chi_{L_\perp}^+ \geq 1$ and $\epsilon^- \propto L_\perp^0$ when $\chi_{L_\perp}^+ < 1$. In both cases, doubling L_\perp doubles δz_{rms}^- in (3.6), and in the strong-turbulence limit this doubles ϵ^- in (3.17). However, in the weak-turbulence limit, doubling L_\perp without changing δz_{rms}^+ , v_A or L_\parallel^+ cuts $\chi_{L_\perp}^+$ in half and leaves ϵ^- in (3.17) unchanged.

Because δz^- fluctuations are generated by the reflection of δz^+ fluctuations and are also sheared by δz^+ fluctuations, δz^- fluctuations are highly coherent in the ‘ δz^+ reference frame,’ which propagates away from the Sun at the group velocity of the δz^+ fluctuations (Velli, Grappin & Mangeney 1989). In particular, in the δz^+ reference frame, the δz^- fluctuations at scale λ remain coherent until the δz^+ fluctuations at scale λ evolve appreciably (LGS07). Lithwick *et al.* (2007) made this last argument for the strong-turbulence regime in which $\chi_\lambda^+ \sim 1$, but the essence of their argument applies equally well to the weak-turbulence regime of reflection-driven turbulence, in which $\chi_\lambda^+ < 1$. In both regimes, if δz^- is infinitesimal so that δz^+ does not evolve via nonlinear interactions, then (neglecting the radial inhomogeneity of the background) δz^+ is constant in the δz^+ frame. As a consequence, δz^- is constant in the δz^+ frame, because δz^- is both generated by δz^+ (via reflection) and cascaded by δz^+ . If, in a thought experiment, one now increases the amplitude of δz^- so that δz^+ evolves via nonlinear interactions, the question arises: How long does one have to wait before the changes in δz^+ give rise to changes in δz^- in the δz^+ frame? Noting that the nonlinear evolution time of δz^+ fluctuations is an increasing function of λ , LGS07 argued that the δz^- fluctuations at scale λ do not evolve in the δz^+ frame until the δz^+ fluctuations at comparable scales have evolved. Prior to such a time, δz^+ fluctuations at scales $\ll \lambda$ will have changed appreciably, but such changes will have little effect upon the δz^- fluctuations at scale λ , which are sensitive primarily

to the reflection of δz^+ fluctuations at scales $\gtrsim \lambda$ and the way that such δz^+ fluctuations cause δz^- fluctuations at scales $\gtrsim \lambda$ to cascade. Therefore, a δz^+ fluctuation at scale λ is sheared coherently by δz^- fluctuations at scale λ throughout the lifetime of the δz^+ fluctuation, and the energy-cascade time scale of δz_λ^+ fluctuations is approximately

$$\tau_{\text{casc},\lambda}^+ = \frac{\lambda}{\delta z_\lambda^-}, \quad (3.18)$$

regardless of the value of χ_λ^- . We refer the reader to LGS07 for a more detailed discussion of this turbulence phenomenology as it plays out in the strong-turbulence regime.

Applying (3.16) and (3.18) to fluctuations at the outer scale, and making use of (3.6) and (3.7), we find the magnetohydrodynamic (MHD) prediction for the rate at which δz^+ energy cascades to smaller scales (cf. Dmitruk *et al.* 2002; Chandran & Hollweg 2009):

$$\epsilon^+ = \frac{m_p n}{4} \left(\frac{U + v_A}{v_A} \right) \left| \frac{\partial v_A}{\partial r} \right|_{\text{eff}} (\delta z_{\text{rms}}^+)^2. \quad (3.19)$$

Just as ϵ^- is independent of L_\perp when $\chi_{L_\perp}^+ < 1$ in the sense described following (3.17), ϵ^+ is independent of L_\perp for fixed U , v_A , $\partial v_A/\partial r$ and δz_{rms}^+ .

3.3. The possibility of weak turbulence at the large-scale end of the inertial range

When $\chi_{L_\perp}^+ < 1$, δz^- fluctuations with $\lambda \sim L_\perp$ are weakly turbulent. In this subsection we describe how we model weak turbulence at the large-scale end of the inertial range when it arises. In the numerical examples in §4, weak turbulence is limited to regions outside the low corona and to a comparatively narrow range of scales near L_\perp for reasons that are explained towards the end of this subsection. As a consequence, the weak-turbulence scalings that we derive here do not have a large impact on our numerical solutions in §4. Nevertheless, we include this discussion for completeness and because, to our knowledge, there are no existing models for the scale dependence of δz_λ^\pm and l_λ^\pm in weak anisotropic reflection-driven turbulence.

To obtain weak-turbulence scalings, we consider the asymptotic weak-turbulence limit, in which

$$\chi_\lambda^+ \ll 1, \quad (3.20)$$

and we take l_λ^- to be the distance a δz^- wave packet at perpendicular scale λ can propagate along the magnetic field during its cascade time scale. It then follows from (3.15) that

$$l_\lambda^- = l_\lambda^+ (\chi_\lambda^+)^{-2}. \quad (3.21)$$

(Setting $\lambda = L_\perp$ in (3.21) implies, via (3.10), that $L_\parallel^- = L_\parallel^+ (\chi_{L_\perp}^+)^{-2}$ when $\chi_{L_\perp}^+ \ll 1$.) Because $l_\lambda^- \gg l_\lambda^+$, the shearing of δz^+ wave packets at perpendicular scale λ by δz_λ^- wave packets at perpendicular scale λ does not reduce the parallel correlation length of the δz^+ wave packets at scale λ , and thus, we set

$$l_\lambda^+ \propto \lambda^0. \quad (3.22)$$

As mentioned following (3.16), in the inertial range, the energy-cascade rate is independent of λ . Upon substituting (3.15) into (3.16) and taking ϵ_λ^- to be independent of λ , we find that

$$\epsilon_\lambda^- = \left(\frac{m_p n}{4} \right) \frac{(\delta z_\lambda^-)^2 (\delta z_\lambda^+)^2 l_\lambda^+}{\lambda^2 v_A} \propto \lambda^0. \quad (3.23)$$

Likewise, after substituting (3.18) into (3.16)⁶ and taking ϵ^+ to be independent of λ , we obtain

$$\epsilon_\lambda^+ = \left(\frac{m_p n}{4}\right) \frac{(\delta z_\lambda^+)^2 \delta z_\lambda^-}{\lambda} \propto \lambda^0. \quad (3.24)$$

Dividing (3.23) by (3.24) and making use of (3.22) yields

$$\delta z_\lambda^- \propto \lambda, \quad (3.25)$$

which corresponds to a perpendicular z^- power spectrum $E^-(k_\perp) \propto k_\perp^{-3}$. Upon substituting (3.25) into either (3.23) or (3.24), we find that

$$\delta z_\lambda^+ \propto \lambda^0, \quad (3.26)$$

which corresponds to a perpendicular z^+ power spectrum $E^+(k_\perp) \propto k_\perp^{-1}$. It then follows from (3.13), (3.22) and (3.26) that

$$\chi_\lambda^+ \propto \lambda^{-1}. \quad (3.27)$$

Equation (3.27) implies that if the turbulence starts out in the weak-turbulence regime at the outer scale with $\chi_{L_\perp}^+ < 1$, then the turbulence transitions to the strong-turbulence regime at $\lambda = \chi_{L_\perp}^+ L_\perp$. For arbitrary values of $\chi_{L_\perp}^+$, the scale

$$\lambda_{\text{str}} = L_\perp \times \min(\chi_{L_\perp}^+, 1) \quad (3.28)$$

then marks the large-scale end of the strongly turbulent part of the inertial range.

3.4. Intermittent, strong MHD turbulence at $\rho_p < \lambda < \lambda_{\text{str}}$

Parker Solar Probe observations reveal that strong turbulence in the near-Sun solar wind is intermittent (Sioulas *et al.* 2024). In intermittent turbulence, the majority of the fluctuation energy at scale λ is concentrated into a fraction of the volume that decreases as λ decreases. Equivalently, as λ decreases, the probability distribution function (PDF) of the fluctuation amplitudes at scale λ broadens, and the tail of this distribution accounts for an increasing fraction of the fluctuation energy at scale λ . Accounting for intermittency is important in solar-wind models because it affects how the turbulent heating power is apportioned between protons and electrons, and between parallel and perpendicular proton heating (Mallet *et al.* 2019), as we will describe in detail in § 3.5.

To model intermittent turbulence, we need a mathematical model for the PDF and how it varies with λ . For this, we adopt the model of Chandran *et al.* (2025), which agrees with a number of PSP observations. In the remainder of this subsection, we summarise the key ideas of this model and the equations from the model that we use in § 3.5 to evaluate the turbulent heating rate.

Chandran *et al.* (2025) considered the Elsasser increments of scale λ at position \mathbf{x} and time t ,

$$\Delta z_\lambda^\pm(\mathbf{x}, \hat{\mathbf{s}}, t) = \mathbf{z}^\pm(\mathbf{x} + 0.5\lambda\hat{\mathbf{s}}, t) - \mathbf{z}^\pm(\mathbf{x} - 0.5\lambda\hat{\mathbf{s}}, t), \quad (3.29)$$

⁶One might expect that a weakly cascaded δz_λ^- would ensure that δz_λ^+ is also weakly cascaded given that $\delta z_{\text{rms}}^+ \gg \delta z_{\text{rms}}^-$. However, we argue that this is not the case in the discussion leading up to (3.18).

where $\hat{\mathbf{s}}$ is a unit vector perpendicular to \mathbf{B} . They then defined the characteristic amplitude of the δz^\pm structure of perpendicular scale λ at position \mathbf{x} and time t to be

$$\delta z_\lambda^\pm(\mathbf{x}, t) = \frac{1}{2\pi} \int_0^{2\pi} d\theta \left| \Delta z_\lambda^\pm(\mathbf{x}, \hat{\mathbf{s}}, t) \right|, \quad (3.30)$$

where the angle θ specifies the direction of $\hat{\mathbf{s}}$ within the plane perpendicular to \mathbf{B} . Rather than considering the detailed \mathbf{x} and t dependence of $\delta z_\lambda^\pm(\mathbf{x}, t)$, Chandran *et al.* (2025) viewed the fluctuations at each λ as a statistical ensemble and treated $\delta z_\lambda^\pm(\mathbf{x}, t)$ (henceforth simply δz_λ^\pm) as a random variable given by

$$\delta z_\lambda^\pm = \bar{z}^\pm \beta^q, \quad (3.31)$$

where β is a constant $\in (0, 1)$, q is a random integer with a Poisson distribution

$$P(q) = \frac{e^{-\mu} \mu^q}{q!} \quad (3.32)$$

and μ is the scale-dependent mean of q . Chandran *et al.* (2025) treated \bar{z}^\pm in (3.31) as a scale-independent random number with an arbitrary distribution, and we simply set

$$\bar{z}^\pm = \delta z_{\text{rms}}^\pm. \quad (3.33)$$

As in previous studies (Grauer, Krug & Marliani 1994; Politano & Pouquet 1995; Mallet & Schekochihin 2017), Chandran *et al.* (2025) determined μ by assuming that the most intense fluctuations (those with $q = 0$) are sheet-like with a volume-filling factor $P(0) \propto \lambda$, obtaining

$$\mu = A + \ln \left(\frac{\lambda_{\text{str}}}{\lambda} \right), \quad (3.34)$$

where A is a constant that determines the breadth of the amplitude distribution at the largest strongly turbulent scale. We set $A = 0$, which, in conjunction with (3.33), amounts to taking the turbulence to be characterised by a single amplitude (rather than a broad distribution) at scale λ_{str} . Qualitatively, as λ decreases, μ increases, causing the distribution of q to broaden, which in turn broadens the PDF of the fluctuation amplitudes.

Chandran *et al.* (2025) solved for β by taking the average δz^+ cascade rate to be independent of λ , obtaining

$$\beta = 2W_0(1/2) = 0.7035, \quad (3.35)$$

where W_0 is the Lambert W function. To obtain (3.35), Chandran *et al.* (2025) assumed that ϵ^+ is dominated by the δz_λ^+ fluctuations in the tail of the distribution (small q values), for which $\delta z_\lambda^+ > w_\lambda^+$, where

$$w_\lambda^\pm = \bar{z}^\pm \beta^\mu = \bar{z}^\pm \left(\frac{\lambda}{\lambda_{\text{str}}} \right)^{-\ln \beta} \quad (3.36)$$

is the approximate median value of δz_λ^\pm . They further argued that, where $\delta z_\lambda^+ > w_\lambda^+$, δz_λ^- can be reasonably approximated as

$$\delta z_\lambda^- = \frac{w_\lambda^- w_\lambda^+}{\delta z_\lambda^+}. \quad (3.37)$$

In (3.37), δz_λ^- is inversely proportional to δz_λ^+ in the tail of the δz_λ^+ distribution because of the strong shearing (and rapid cascading) experienced by δz_λ^- where δz_λ^+ is large. The average δz^+ cascade power at scale λ is then approximately

$$\langle \epsilon_\lambda^+ \rangle = \sum_{q=0}^{\infty} P(q) \frac{m_p n (\delta z_\lambda^+)^2 \delta z_\lambda^-}{4\lambda} = \sum_{q=0}^{\infty} P(q) \epsilon_{\lambda,q}^+, \quad (3.38)$$

where

$$\epsilon_{\lambda,q}^+ = \frac{m_p n (\bar{z}^+)^2 \bar{z}^-}{4\lambda} \left(\frac{\lambda}{\lambda_{\text{str}}} \right)^{-2 \ln \beta} \beta^q. \quad (3.39)$$

Equations (3.38) and (3.39) quantify how much each part of the PDF of δz_λ^+ contributes to $\langle \epsilon_\lambda^+ \rangle$. To determine the parallel length scales of the AW packets, Chandran *et al.* (2025) applied the arguments of LGS07 to intermittent turbulence, setting

$$l_\lambda^+ = l_\lambda^- = \frac{v_A \lambda}{\delta z_\lambda^+} \quad (3.40)$$

throughout the δz_λ^+ distribution.

3.5. The turbulent heating rate

We make the simplifying assumption that all dissipation takes place either at $\lambda \sim \rho_p$ (proton-gyroscale dissipation) or at $\lambda \ll \rho_p$ (sub-proton-scale dissipation). We note that $\tau_{\text{casc},\lambda}^- \ll \tau_{\text{casc},\lambda}^+$ and assume that $\tau_{\text{casc},\lambda}^-$ is much smaller than the dissipation time scale of δz^- fluctuations at $\lambda \sim \rho_p$. Given this assumption, ϵ^- cascades past $\lambda \sim \rho_p$ and dissipates almost entirely at $\lambda \ll \rho_p$, heating only the electrons. We take the perpendicular proton heating rate $Q_{\perp p}$ to be the rate at which stochastic proton heating (e.g. McChesney, Stern & Bellan 1987) removes energy from δz^+ fluctuations at $\lambda \sim \rho_p$, and we equate $Q_{\parallel p}$ with the rate at which proton Landau damping (LD) and transit-time damping (TTD) remove energy from δz^+ fluctuations at $\lambda \sim \rho_p$. We define Q_{e1} to be the rate at which electron LD and TTD remove energy from δz^+ fluctuations at $\lambda \sim \rho_p$ and take the total electron heating rate to be

$$Q_e = Q_{e1} + Q_{e,\text{sub-proton}}, \quad (3.41)$$

where

$$Q_{e,\text{sub-proton}} = \epsilon^- + \epsilon^+ - Q_{\perp p} - Q_{\parallel p} - Q_{e1} \quad (3.42)$$

is the rate at which energy cascades past the proton gyroradius scale to $\lambda \ll \rho_p$.

As a preliminary step towards evaluating $Q_{\perp p}$, $Q_{\parallel p}$ and Q_{e1} , we relate λ and l_λ^+ to characteristic perpendicular and parallel wavenumbers, k_\perp and k_\parallel (k_\perp), using the relations suggested by figure 1 of Huang *et al.* (2023):

$$k_\perp = \frac{\pi}{\lambda}, \quad k_\parallel(k_\perp) = \frac{\pi}{l_\lambda^\pm}. \quad (3.43)$$

As described further in the following, we evaluate the proton-gyroscale heating rates using the properties of the turbulence at

$$k_\perp \rho_p = 1 \quad \longleftrightarrow \quad \lambda = \pi \rho_p. \quad (3.44)$$

Equation (3.43) and the critical-balance relation (3.40) imply that

$$k_{\parallel}(\rho_p^{-1})v_A = \frac{\pi v_A}{l_{\pi\rho_p}} = \frac{\pi\delta z_p^+}{\pi\rho_p} = \frac{\delta z_p^+}{\rho_p}, \quad (3.45)$$

where δz_p^+ is the value of δz_{λ}^+ at $\lambda = \pi\rho_p$. Although fluctuations at $k_{\perp}\rho_p = 1$ are at the transition between MHD scales and kinetic scales, we approximate these fluctuations using results from MHD. In particular, we assume that the PDF of δz_p^+ is given by (3.31), (3.32) and (3.34) with $\lambda = \pi\rho_p$, that the energy density of these fluctuations is $m_p n (\delta z_p^+)^2 / 4$, and that the amplitude of the fluctuating electron fluid velocity (or $\mathbf{E} \times \mathbf{B}$ velocity) associated with the δz_p^+ fluctuations at $k_{\perp}\rho_p = 1$ is given by

$$\delta v_p = \frac{1}{2}\delta z_p^+. \quad (3.46)$$

We define $\gamma_p(k_{\perp})$ and $\gamma_e(k_{\perp})$ to be the rates at which (kinetic) AWs at perpendicular wavenumber k_{\perp} and parallel wavenumber $k_{\parallel}(k_{\perp})$ lose energy to linear LD/TTD via interactions with protons and electrons, respectively. We adopt the analytic expressions for $\gamma_p(k_{\perp})$ and $\gamma_e(k_{\perp})$ derived by Howes *et al.* (2006) within the gyrokinetics approximation for the case in which $m_e T_p / (m_p T_e) \ll \beta_p \ll 1$, simplified to the limit in which $k_{\perp}\rho_e \ll 1$, where ρ_e is the electron gyroradius:

$$\gamma_e(k_{\perp}) = \frac{\pi^{1/2}}{2} \left(\frac{\alpha_p^2 m_e T_e}{m_p T_p \beta_p} \right)^{1/2} |k_{\parallel}(k_{\perp})| v_A \quad (3.47)$$

and

$$\gamma_p(k_{\perp}) = \frac{\pi^{1/2}}{2} \frac{\alpha_p T_e^2}{\beta_p^{1/2} T_p^2} e^{-\alpha_p - \bar{\omega}^2 \beta_p^{-1}} I_0(\alpha_p) |k_{\parallel}(k_{\perp})| v_A, \quad (3.48)$$

where

$$\alpha_p = \frac{1}{2} (k_{\perp}\rho_p)^2, \quad \beta_p = \frac{8\pi n k_B T_p}{B^2}, \quad (3.49)$$

T_p is defined in (2.18), $I_0(x)$ is the modified Bessel function of the first kind of order 0 and $\bar{\omega} = \omega / (k_{\parallel} v_A)$. Like δz_p^+ , $\gamma_e(\rho_p^{-1})$ and $\gamma_{\parallel p}(\rho_p^{-1})$ are functions of q via (3.45).

Using these linear damping rates, we define hypothetical rates $\Gamma_{e,q}$ and $\Gamma_{\parallel p,q}$ at which electrons and protons, respectively, would drain energy from δz_{λ}^+ fluctuations at $\lambda = \pi\rho_p$ (i.e. δz_p^+ fluctuations) with a given value of q in (3.31) via LD and TTD if the fluctuation amplitudes were unaffected by this energy transfer:

$$\Gamma_{e,q} = \frac{c_{LD}}{2} \gamma_e(\rho_p^{-1}) m_p n (\delta z_p^+)^2 \quad (3.50)$$

and

$$\Gamma_{\parallel p,q} = \frac{1}{2} \gamma_{\parallel p}(\rho_p^{-1}) m_p n (\delta z_p^+)^2, \quad (3.51)$$

where the constant c_{LD} is a free parameter that enables us to modify the effective electron LD rate.⁷ In writing (3.50) and (3.51), we have accounted for the fact that

⁷We have not included such a parameter in (3.51) because parallel proton heating is negligible in the numerical examples presented in § 4.

the energy damping rate is twice the amplitude damping rate. For perpendicular proton heating, we define $\Gamma_{\perp p,q}$ to be the hypothetical rate at which δz_p^+ fluctuations would cause stochastic perpendicular proton heating if there were no reduction of δz_p^+ by dissipation at $k_{\perp} \rho_p \sim 1$. Following Chandran *et al.* (2010), we set

$$\Gamma_{\perp p,q} = \frac{m_p n \delta v_p^3}{\rho_p} \exp\left(-\frac{c_2 v_{\perp th,p}}{\delta v_p}\right), \quad (3.52)$$

where c_2 is an adjustable parameter, and we have set $c_1 = 1$ in equation (25) of Chandran *et al.* (2010) to reduce the number of free parameters in our model.⁸

To go beyond the hypothetical heating rates in (3.50) through (3.52), we need to account for the feedback of the damping/dissipation process on the proton-gyroscale fluctuations, which prevents the proton-gyroscale turbulent heating rate from exceeding the rate at which energy cascades through the inertial range. We do so by taking the contribution of the δz_{λ}^+ fluctuations at $\lambda = \pi \rho_p$ with a given value of q in (3.31) to $Q_{\perp p}$, $Q_{\parallel p}$ and Q_{e1} to be, respectively,

$$Q_{\perp p,q} = \frac{\Gamma_{\perp p,q} \epsilon_{p,q}^+}{\epsilon_{p,q}^+ + \Gamma_{\perp p,q} + \Gamma_{\parallel p,q} + \Gamma_{e,q}}, \quad (3.53)$$

$$Q_{\parallel p,q} = \frac{\Gamma_{\parallel p,q} \epsilon_{p,q}^+}{\epsilon_{p,q}^+ + \Gamma_{\perp p,q} + \Gamma_{\parallel p,q} + \Gamma_{e,q}} \quad (3.54)$$

and

$$Q_{e1,q} = \frac{\Gamma_{e,q} \epsilon_{p,q}^+}{\epsilon_{p,q}^+ + \Gamma_{\perp p,q} + \Gamma_{\parallel p,q} + \Gamma_{e,q}}, \quad (3.55)$$

where $\epsilon_{p,q}^+$ is the value of $\epsilon_{\lambda,q}^+$ in (3.39) with $\lambda = \pi \rho_p$, which is the rate at which the energy cascade replenishes the energy of the fluctuations with a given value of q at $\lambda = \pi \rho_p$. If $\Gamma_{\perp p,q} + \Gamma_{\parallel p,q} + \Gamma_{e,q}$ is $\ll \epsilon_{p,q}^+$, then the energy drained from fluctuations at $k_{\perp} \rho_p \sim 1$ has a negligible effect on their amplitudes, and (3.53) through (3.55) imply that $Q_{\perp p,q} \simeq \Gamma_{\perp p,q}$, $Q_{\parallel p,q} \simeq \Gamma_{\parallel p,q}$ and $Q_{e1,q} \simeq \Gamma_{e,q}$. Conversely, if $\Gamma_{\perp p,q} + \Gamma_{\parallel p,q} + \Gamma_{e,q} \gg \epsilon_{p,q}^+$ then the energy drained from the proton-gyroscale fluctuations strongly modifies their amplitudes and $Q_{\perp p,q} \ll \Gamma_{\perp p,q}$, $Q_{\parallel p,q} \ll \Gamma_{\parallel p,q}$ and $Q_{e1,q} \ll \Gamma_{e,q}$. In this regime, (3.53) through (3.55) imply that $Q_{\perp p,q} + Q_{\parallel p,q} + Q_{e1,q} \simeq \epsilon_{p,q}^+$, $Q_{\perp p,q}/Q_{\parallel p,q} = \Gamma_{\perp p,q}/\Gamma_{\parallel p,q}$ and $Q_{\perp p,q}/Q_{e1,q} = \Gamma_{\perp p,q}/\Gamma_{e,q}$. The total heating rates from the full distribution of proton-gyroscale fluctuations are

$$Q_{\perp p} = \sum_{q=0}^{\infty} P(q) Q_{\perp p,q}, \quad Q_{\parallel p} = \sum_{q=0}^{\infty} P(q) Q_{\parallel p,q}, \quad Q_{e1} = \sum_{q=0}^{\infty} P(q) Q_{e1,q}. \quad (3.56)$$

We emphasise that the turbulent heating described by (3.50) through (3.56) results entirely from fluctuations at $\lambda = \pi \rho_p$. We neglect turbulent heating from larger-scale fluctuations and model the turbulent heating from smaller-scale fluctuations via (3.42).

⁸The constant c_1 is an overall normalisation factor on the right-hand side of (3.52). For reference, Chandran *et al.* (2010) fit their (25) to test-particle simulations of proton stochastic heating by randomly phased AWs and KAWs and obtained $c_1 = 0.75$.

4. Numerical examples

In this section we present numerical solutions to (2.5) through (2.12). We use the implicit algorithm of Hu, Esser & Habbal (2000) with an adaptive time step to advance the equations forward in time until a steady state is reached. All the plots in this section illustrate steady-state solutions. The innermost grid point, $r = r_b$, in these solutions is approximately 2000 km above the photosphere. At the inner boundary, we take the three temperatures $T_{\perp p}(r_b)$, $T_{\parallel p}(r_b)$ and $T_e(r_b)$ to equal

$$T(r_b) = 10^5 \text{ K}, \quad (4.1)$$

and we fix the proton number density and AW energy density at the values

$$n(r_b) = 10^9 \text{ cm}^{-3}, \quad \mathcal{E}_w(r_b) = 5.74 \times 10^{-3} \text{ erg cm}^{-3}. \quad (4.2)$$

Our choice of $T(r_b)$ is somewhat arbitrary. We find that the precise value of $T(r_b)$ does not significantly alter the solutions provided that $T(r_b) \ll 10^6 \text{ K}$ and that we vary $T(r_b)$ and $n(r_b)$ together, keeping $n(r_b)T(r_b)$ constant. We choose the value of $n(r_b)T(r_b)$ to approximately match observational constraints on the density in the low corona from Allen (1973), which are plotted in figure 4. Our choice of $\mathcal{E}_w(r_b)$ leads to reasonable agreement with the observational constraint on δv_{rms} in the low corona from the Hinode spacecraft (De Pontieu *et al.* 2007), which is shown in figure 4. We determine $U(r_b)$, $q_{\perp p}(r_b)$, $q_{\parallel p}(r_b)$ and all the variables at the outermost grid point by linear extrapolation from the nearest two grid points.

4.1. Magnetic-field model and radial grid

All the examples presented in this section are based on the same axisymmetric magnetic-field model, which is designed to emulate the solar and heliospheric magnetic field near the minimum of the solar cycle. Following Cranmer *et al.* (2007), we start with the dipole-plus-quadrupole-plus-current-sheet model of Banaszkiewicz *et al.* (1998), adopting the latter authors' favoured parameters of $K = 1$, $M = 1.789$, $a_1 = 1.538$ and $Q = 1.5$. We then add to this model the low-solar-atmosphere magnetic-field model of Hackenberg *et al.* (2000) using the parameters from their figure 1: $L = 3 \times 10^9 \text{ cm}$, $d = 3.4 \times 10^7 \text{ cm}$ and $B_{\text{max}} = 1.5 \text{ kG}$. We illustrate the magnetic-field lines in this Banaszkiewicz–Hackenberg (B-H) model in figure 2(a).

Our solar-wind model applies to narrow magnetic flux tubes directed radially outwards from the Sun and does not take into account the curvature of magnetic-field lines. In order to approximate the B–H magnetic-field structure with our radial magnetic flux tubes, we compute B as a function of arc length s in the B–H model along a number of magnetic-field lines that intersect the Sun at spherical polar angles θ_\odot and that reach heliolatitudes Θ_{60R_\odot} at a heliocentric distance $r = 60R_\odot$, where the heliolatitude is 90° minus the spherical polar angle. For example, $\theta_\odot = 0$ and $\Theta_{60R_\odot} = 90^\circ$ both correspond to the radial magnetic-field line connected to the Sun's north pole. We also compute the function $r(s)$, the heliocentric distance as a function of arc length, along these field lines as well as the inverse of this function, $s(r)$. We then compose the function $B(r) = B(s(r))$ for each of these field lines and solve (2.5) through (2.12) within radial magnetic flux tubes that have the same $B(r)$ profiles. Figure 2(b) shows the $B(r)$ profiles for three different values of θ_\odot , which correspond to the three values of Θ_{60R_\odot} listed in the figure. In the figures to follow, we label our model solutions by the Θ_{60R_\odot} value of the B–H magnetic-field line that our model attempts to emulate, but we omit the $60R_\odot$ subscript to simplify the figure legends.

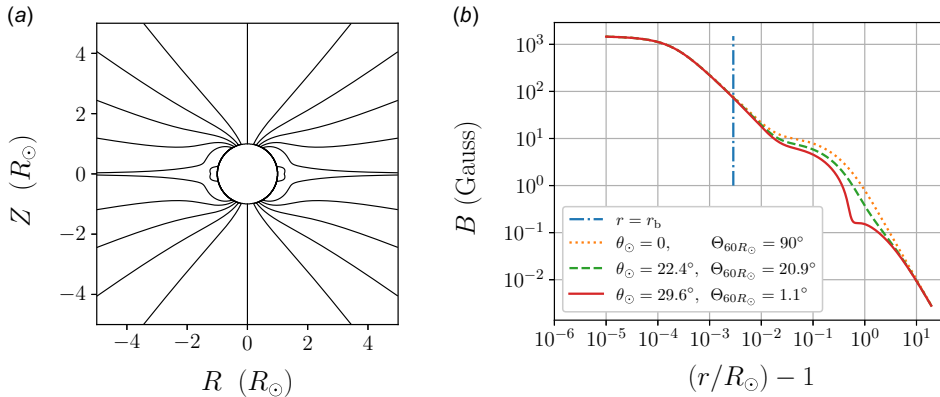


FIGURE 2. (a) Magnetic-field lines in the axisymmetric, solar-minimum, B-H magnetic-field model (Banaszkiewicz *et al.* 1998; Hackenberg *et al.* 2000). (b) The magnetic-field strength B as a function of heliocentric distance r along three different B-H magnetic-field lines that intersect the Sun at spherical polar angle θ_\odot and that connect to heliolatitudes Θ_{60R_\odot} at $r = 60R_\odot$. We use these $B(r)$ profiles for the radial magnetic flux tubes in our 1-D solar-wind model to emulate magnetic-field lines in the 2-D B-H model. The vertical line shows the minimum radius r_b in our solar-wind model.

To construct our numerical grid of r values, we first take $N = 1002$ points that are evenly spaced in the variable $\ln((s - R_\odot)/R_\odot)$ between a minimum value of $\ln(2000 \text{ km}/R_\odot)$ and a maximum value of $\ln(71)$. These N points correspond to N arclengths s_j , with j ranging from 1 to N , which we convert into N heliocentric distances r_j by setting $r_j = r(s_j)$. The resulting r_j values range from approximately $R_\odot + 2000 \text{ km}$ to $72R_\odot$. The spacing between neighbouring grid points increases from $\simeq 20 \text{ km}$ near the inner edge of the grid to $\simeq 5 \times 10^5 \text{ km}$ near the outer edge of the grid.

4.2. Parameter values

We focus on the set of parameters listed in table 1. We follow van Ballegoijen & Asgari-Targhi (2016) in viewing the open magnetic flux in the heliosphere as originating primarily in magnetic flux tubes that, at the photosphere, have diameters $\simeq 100 \text{ km}$ and magnetic-field strengths $\simeq 1 \text{ kG}$. These flux tubes cover approximately 1 % of the photosphere but expand and merge in the low corona, where $B \simeq 10 \text{ G}$ and the flux tubes fill most of the volume. By flux conservation, the diameters of the flux tubes are $\simeq 10^3 \text{ km}$ in the low corona. Photospheric motions at the base of these flux tubes launch waves that propagate outwards through the chromosphere and into the corona. Because the motions of different flux tubes are uncorrelated at the photosphere, the motions of different flux tubes are largely uncorrelated in the corona. We therefore set $L_{\perp \text{kG}} = 100 \text{ km}$. It follows from (3.8) that this choice of $L_{\perp \text{kG}}$ corresponds to a perpendicular correlation length $L_\perp(r)$ that is 10^3 km in the low corona where $B \simeq 10 \text{ G}$. We note that a very similar value of $L_{\perp \text{kG}}$ (90.9 km) in the AW-driven solar-wind model of Cranmer *et al.* (2007) led to good agreement with measurements of the Faraday rotation of linearly polarised radio transmissions from the Helios spacecraft (Hollweg, Cranmer & Chandran 2010).

We determine the remaining parameters approximately as follows. We choose c_{refl} to match observations of T_e in the low corona, and we then adjust c_{LD} and c_2

Parameter	Value	Physical significance
$L_{\perp kG}$	100 km	\perp correlation length of turbulence where $B = 1$ kG
c_{refl}	0.15	Upper limit on $\delta z_{\text{rms}}^- / \delta z_{\text{rms}}^+$ in the low corona
c_{LD}	0.2	Reduction factor in the electron LD rate
c_2	0.15	Coefficient in the exponent of the stochastic-heating rate
α_{H}	0.2	Coefficient in Hollweg's collisionless-heat-flux formula
r_{H}	$4R_{\odot}$	Radius of transition from Spitzer to Hollweg heat flux

TABLE 1. Parameter Values.

together to match observational constraints on $U(r)$ at large r and large Θ from the Ulysses spacecraft (see §4.3), as well as observational constraints on $T_{\perp p}$ at large r from PSP's tenth perihelion encounter (E10) from 18 November 2021 until 21 November 2021 (see §4.4). We then adjust α_{H} and r_{H} to improve slightly the agreement between the model and observational constraints on T_e from PSP during E10 (see §4.4).

Although it is our variation of the parameters c_{refl} , c_{LD} , c_2 , α_{H} and r_{H} that enables our model to match the observations described in the previous paragraph, our model agrees with other observations without the need for further parameter adjustment. These observations include the latitudinal dependence of U at large r and the radial profiles of n , δv_{rms} and $T_{\parallel p}$ seen by PSP during E10, as we discuss in §§4.3 and 4.4.

4.3. Comparison with Ulysses measurements of $U_{\infty}(\Theta)$ near solar minimum

Because the radiative cooling rate is $\propto n^2$, radiative cooling is only important in our model in the low corona.⁹ In steady state outside the low corona, both $a(r)F_{\text{tot}}(r)$ and $a(r)\rho(r)U(r)$ are independent of r , and thus, $F_{\text{tot}}(r)/[\rho(r)U(r)]$ is independent of r , where F_{tot} is the total energy flux defined in (2.21). Asymptotically far from the Sun, almost all of the solar-wind energy flux is in the form of bulk-flow kinetic energy, and the wind speed is approximately

$$U_{\infty} = \left[\frac{2F_{\text{tot}}(r)}{\rho(r)U(r)} \right]^{1/2}, \quad (4.3)$$

where the right-hand side of (4.3) can be evaluated at any r far outside the low corona. In figure 3(a) we plot U_{∞} as a function of heliolatitude Θ in our model as well as measurements of U from the first polar orbit of the Ulysses spacecraft in 1994–1995, near the minimum of the solar cycle. Notably, our model reproduces the observed decrease in the outflow velocity as $|\Theta|$ drops to $\lesssim 20^\circ$. The reason for this reduction is that, at $|\Theta| \lesssim 20^\circ$, there is a large drop in B as r increases from $\simeq 1.2R_{\odot}$ to $\simeq 1.6R_{\odot}$, as illustrated in figure 2. This drop in B leads to a large Alfvén-speed gradient, which enhances the turbulent heating rate via (3.19). This enhanced heating rate increases the temperature, which increases the density scale height, causing more mass to be loaded into the corona out to the sonic critical point (at a heliocentric distance of a few R_{\odot}). This, in turn, increases the mass

⁹This statement is quantified in figures 5(b) and 8(f).

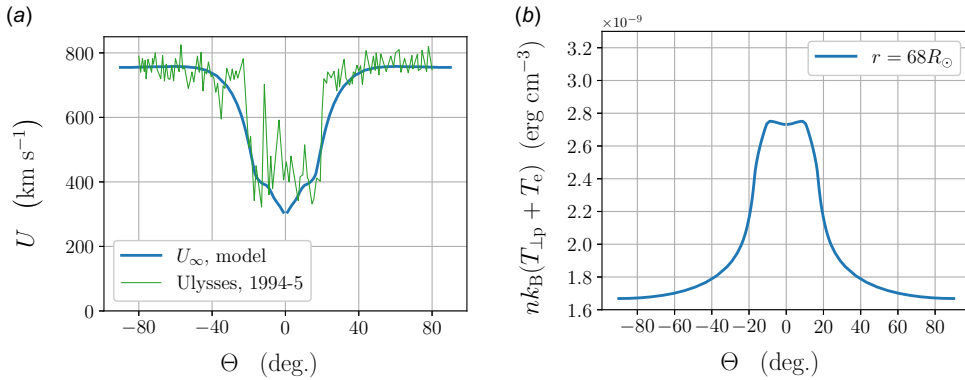


FIGURE 3. (a) The asymptotic solar-wind speed U_∞ defined in (4.3) as a function of heliolatitude Θ and the solar-wind speed measured by the Ulysses spacecraft during its first polar orbit in 1994 and 1995 (Goldstein *et al.* 1996). (b) The transverse pressure at $r = 68 R_\odot$ in our model as a function of Θ .

loss rate of the solar wind (Hansteen & Velli 2012), causing the total energy budget to be shared by more particles, which reduces U_∞ (cf. Leer & Holzer 1980; Chandran 2021).

Cranmer *et al.* (2007) and Lionello *et al.* (2014a) developed 1-D AW-driven solar-wind models and used the same Banaszkiewicz *et al.* (1998) magnetic-field model that we have used to model solar-wind streams at different heliolatitudes. In the study by Lionello *et al.* (2014a), the drop in $U_\infty(\Theta)$ and increase in thermal pressure near the ecliptic were more sharply peaked at small Θ than in figure 3. In the study by Cranmer *et al.* (2007), the drop in $U_\infty(\Theta)$ and change in thermal pressure were likewise more sharply peaked at small Θ than in figure 3, but the thermal pressure decreased at small Θ . Lionello *et al.* (2014a) pointed out that pressure differentials across the magnetic field lead to a loss of transverse force balance, and that, in a more realistic two-dimensional (2-D) or 3-D model, the high-pressure region would expand into the low-pressure region, thereby modifying the magnetic-field profiles. To obtain an order-of-magnitude estimate of the importance of this effect, we note that the increment in Θ through which a high-pressure region can expand during the time $\sim r/U$ it takes the wind to reach heliocentric distance r is approximately $\Delta\Theta = (r/U) \times (\Delta c_s/r) = \Delta c_s/U$ radians, where Δc_s is the change in sound speed over the heliolatitude interval $\Delta\Theta$. An upper limit on $\Delta\Theta$ is obtained by setting $\Delta c_s = c_s$, in which case $\Delta\Theta = c_s/U = 1/M$, where M is the sonic Mach number. As $M \gtrsim 10$ at large r , this upper limit on $\Delta\Theta$ is $\lesssim 5.7^\circ$. However, the pressure differential over 5.7° in figure 3 is only a fraction of the full pressure, and so the actual value of $\Delta\Theta$ is significantly less than 5.7° . We thus conjecture that the meridional expansion of the slow-wind region that would arise in a 2-D or 3-D version of our model would be comparatively modest.

4.4. Comparison with PSP E10 observations

During the approach phase of PSP's tenth perihelion encounter with the Sun (E10), the spacecraft travelled approximately radially in the Sun's rotating frame for $\simeq 20 R_\odot$, remaining within a single solar-wind stream that was magnetically connected to a small low-latitude coronal hole (Davis *et al.* 2023). This 'fast radial scan'

provided a good opportunity to measure the radial variation of the solar-wind properties within the same magnetic flux tube, and we therefore compare our model results with PSP E10 data. A problem with doing so, however, is that the low-latitude coronal hole from which this wind stream emerged was a non-axisymmetric structure that is not captured by the axisymmetric B–H magnetic-field model. To compare our model with PSP E10 observations, we assume that the $B(r)$ profile along the magnetic flux tube encountered by PSP is similar to the $B(r)$ profile along the magnetic-field lines in our model along which $U_\infty \simeq 550 \text{ km s}^{-1}$ (a value slightly above the proton outflow velocity measured by PSP during E10). We then compare PSP E10 observations with our model solution along one of these field lines: the one that reaches heliolatitude $\Theta = 20.9^\circ$ at large r , for which $U_\infty = 541 \text{ km s}^{-1}$.

In [figure 4](#) we plot our numerical solutions for n , U , $T_{\perp p}$, $T_{\parallel p}$, T_e , $\beta_{\parallel p}$, $\chi_{L\perp}^+$ and the ratio of the electron Coulomb mean free path

$$\lambda_{\text{mfp}} \equiv \frac{\sqrt{k_B T_e / m_e}}{v_e} \quad (4.4)$$

to r , where

$$v_e = 2.9 \times 10^{-6} \left(\frac{n}{1 \text{ cm}^{-3}} \right) \left(\frac{k_B T_e}{1 \text{ eV}} \right)^{-3/2} \ln \Lambda \text{ s}^{-1} \quad (4.5)$$

is the electron collision frequency and $\ln \Lambda$ is the Coulomb logarithm defined following (2.15) (Book 1983). The vertical dotted line in [figure 4\(b\)](#) indicates the radius inside of which the Alfvén-speed gradient is so large that δz_{rms}^- is limited to the value $c_{\text{refl}}(U + v_A)/v_A$ via (3.6) and (3.7). The PSP n and T_e data in [figure 4](#) are taken from the SPAN-E instrument (Whittlesey *et al.* 2020) of the Solar Wind Electrons, Alphas and Protons (SWEAP) instrument suite (Kasper *et al.* 2016), and the velocity and proton-temperature data are taken from SWEAP’s SPAN-I instrument (Livi *et al.* 2022). The overall calibration of the SPAN-E density measurements is obtained by comparing with quasithermal-noise measurements of the electron density (Moncuquet *et al.* 2020) from the PSP FIELDS instrument suite (Bale *et al.* 2016). We also plot in [figure 4](#) remote observations of $T_{\perp p}$ from UVCS (Esser *et al.* 1999), T_e from SUMER (Landi 2008), δv_{rms} from Hinode (De Pontieu *et al.* 2007) and n from white-light scattering in coronal holes (Allen 1973). We note, however, that the UVCS, SUMER and white-light-scattering observations are for large polar coronal holes (the source regions of fast solar wind with $U_\infty \simeq 750 \text{ km s}^{-1}$), which may differ from the small low-latitude coronal hole that produced the wind stream observed by PSP during E10.

Our model solution is in broad, but not complete, agreement with these observations. The most notable differences are that (1) $T_{\perp p}$ in the model is smaller than the (polar-coronal-hole) value observed by UVCS at $1.3R_\odot < r < 1.8R_\odot$; and (2) T_e in the model is higher than in the PSP observations, particularly near $r = 15R_\odot$.

Beyond the comparison with observations, [figure 4\(f\)](#) shows that (1) δz^- fluctuations transition out of the strong-turbulence regime as r increases past $\simeq 2R_\odot$; (2) the low corona is highly collisional, with $\lambda_{\text{mfp}} \ll r$, whereas the outer corona and solar wind are only weakly collisional, with $\lambda_{\text{mfp}} \gtrsim r$; and (3) $\beta_{\parallel p}$ is $\lesssim 0.1$ at $r < 20R_\odot$ but increases with increasing r , reaching a value $\simeq 1$ by $r = 50R_\odot$.

[Figure 5](#) shows several diagnostics of the heating and energy flow in this solution. [Figure 5\(a\)](#) shows that electron LD at $\lambda \sim \rho_p$ is the dominant heating mechanism at $r \lesssim 2R_\odot$, that stochastic proton heating is the dominant heating mechanism at $r \gtrsim 2R_\odot$, and that dissipation at sub-proton scales and parallel proton heating

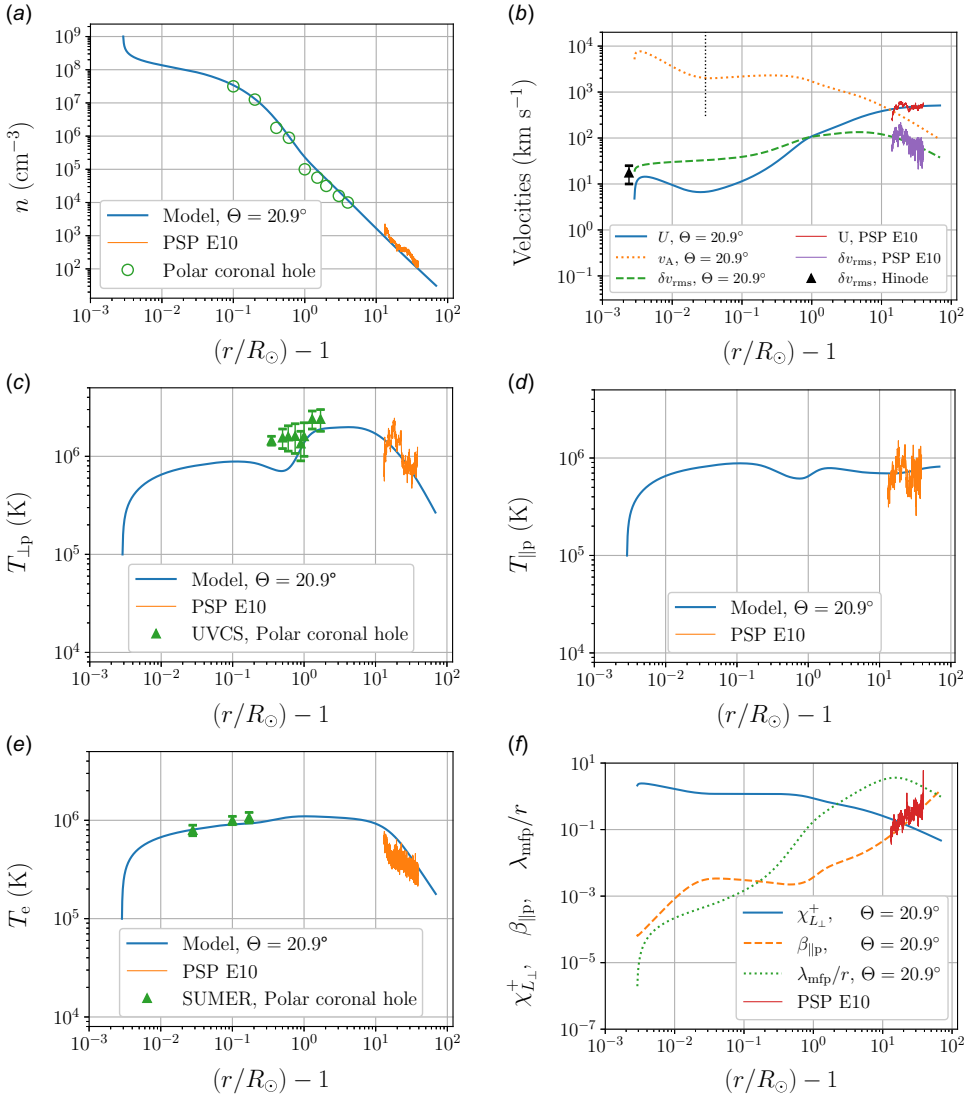


FIGURE 4. Radial profiles of several quantities in our model solution that reaches heliolatitude $\Theta = 20.9^\circ$ at large r : n is the proton number density, U is the solar-wind outflow velocity, v_A is the Alfvén speed, δv_{rms} is the r.m.s. fluctuating velocity, $T_{\perp p}$ and $T_{\parallel p}$ are the perpendicular and parallel proton temperatures, T_e is the electron temperature, $\chi_{L\perp}^+$ is the outer-scale critical-balance parameter defined in (3.13), $\beta_{\parallel p}$ is the parallel proton beta and λ_{mfp} is the electron Coulomb mean free path. The vertical dotted line in panel (b) is described in the text.

are subdominant at all r . The reason that parallel proton heating is negligible at $r \lesssim 15R_\odot$ is that it requires a Landau resonance between the waves and the ions, in which the parallel ion velocity (along \mathbf{B}) matches the parallel wave phase velocity. However, the parallel thermal speed is $\beta_{\parallel p}^{1/2} v_A$, and $\beta_{\parallel p} < 0.1$ at $r \lesssim 15R_\odot$, as shown in figure 4(f), implying that the large majority of the protons are much slower than the AWs and kinetic Alfvén waves (KAWs), whose parallel phase velocities are $\geq v_A$. The reason that the stochastic proton heating rate $Q_{\perp p}$ becomes relatively

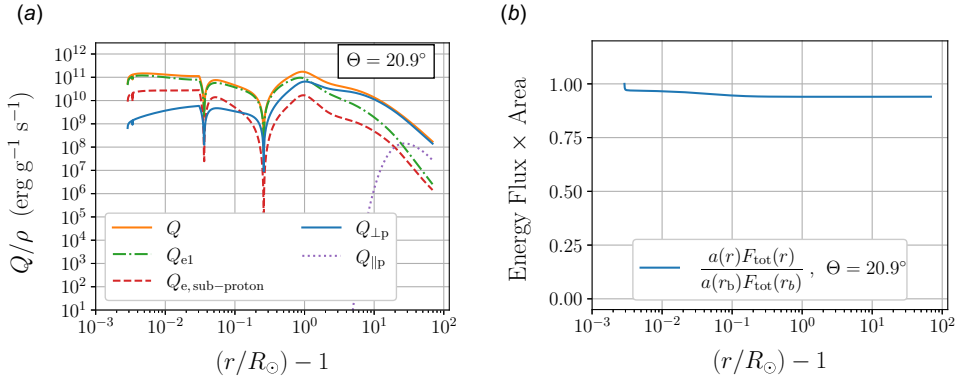


FIGURE 5. (a) Heating and cascade rates divided by the mass density ρ : Q is the total heating rate; Q_{el} ($Q_{\parallel p}$) is the rate at which electron (proton) LD/TTD drain energy from fluctuations at $k_\perp \rho_p \sim 1$; $\epsilon_{\text{sub-proton}}$ is the energy-cascade rate at $k_\perp \rho_p > 1$; and $Q_{\perp p}$ is the proton stochastic heating rate. (b) The total energy flux $F_{\text{tot}}(r)$ defined in (2.21) multiplied by the cross-sectional area of the flow $a(r)$ normalised to the value of this product at the inner radius of the model r_b .

more important in comparison to the parallel electron heating rate as r increases above $\simeq 2R_\odot$ is that $Q_{\perp p}$ is a rapidly increasing function of $\delta v_{\text{rms}}/v_A$ because of the exponential in (3.52). As illustrated in figure 4(b), $\delta v_{\text{rms}}/v_A$ increases monotonically from $< 10^{-2}$ in the low corona to $\simeq 1/4$ at $r = 10R_\odot$.

A comparison between figure 5(a) and figure 4(b) shows that the heating rate vanishes at the local extrema of $v_A(r)$. This feature of our model results from the fact that we have estimated δz_{rms}^- in (3.6) using only the local value of $|\partial v_A/\partial r|$, which determines the local rate of reflection. In coronal holes and the solar wind, after δz^- fluctuations are produced by reflection, they propagate some distance before cascading and dissipating, and δz_{rms}^- should not vanish anywhere. It would be possible to smooth out the δz_{rms}^- and Q profiles, but we have opted not to do so, as the vanishing of Q at these locations does not lead to sharp features in the temperature profiles and because smoothing would introduce an additional free parameter (the smoothing length).

In figure 5(b) we plot the product of the total energy flux $F_{\text{tot}}(r)$ and the area of the flow $a(r)$. This product should be constant in steady state in the absence of radiative cooling, as per (2.19). The fact that $a(r)F_{\text{tot}}(r)$ is approximately constant at $r \gtrsim 1.2R_\odot$ in figure 5 shows that radiative cooling plays a role only in the low solar corona. The sharp drop in $a(r)F_{\text{tot}}(r)$ at the left of the plot represents a decrease in the total energy flux of $\simeq 3\%$ over a distance of $\simeq 130$ km. Although this abrupt drop has the appearance of a possible artefact associated with the boundary condition and the neighbouring grid cell, the drop is in fact resolved across $\simeq 7$ grid cells and coincides with the large drop in the density (by a factor of $\simeq 2.5$) over this same radial interval. We interpret this abrupt drop as an approximation of the physical cooling that occurs near the top of the transition region.

Figure 6(a) shows the PDF of the integer q in (3.31), evaluated for δz_λ^+ at $\lambda = \pi\rho_p$ (i.e., the PDF of $\log_\beta(\delta z_p^+/\bar{z}^+)$). Figure 6(b) shows the contributions of the different parts of the δz_p^+ distribution to $Q_{\perp p}$ and Q_{el} (which are, respectively, the stochastic proton heating rate and the rate at which electrons are heated by LD/TTD of Alfvénic fluctuations at the proton gyroscale). As these panels show, stochastic proton heating results mainly from the large-amplitude end of the distribution, whereas

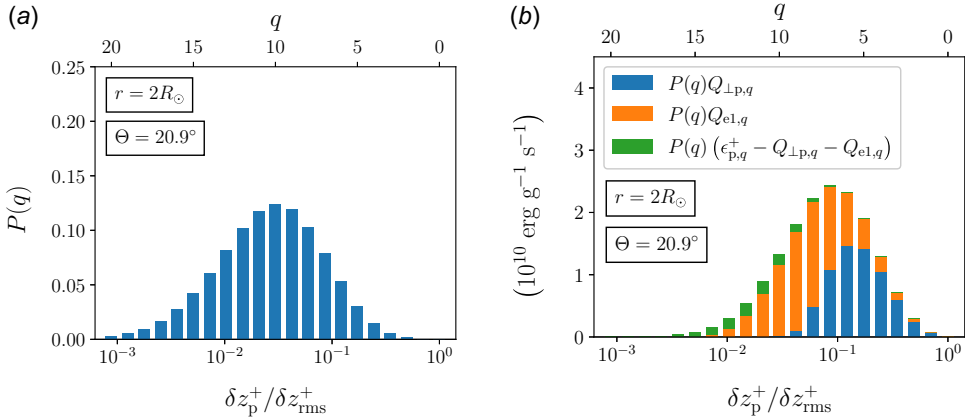


FIGURE 6. (a) The quantity $P(q)$ is the PDF of the integer q in the equation for the proton-gyroscale fluctuation amplitude $\delta z_p^+ = (0.7035)^q \delta z_{rms}^+$ (see § 3.4), where δz_p^+ is the value of δz_λ^+ at $\lambda = \pi \rho_p$. The top and bottom axes show q and the corresponding value of $\delta z_p^+ / \delta z_{rms}^+$. (b) The quantities $P(q)Q_{\perp,q}$ and $P(q)Q_{e1,q}$ show, respectively, the contribution to the perpendicular proton heating rate and electron heating rate from each part of the distribution of fluctuation amplitudes at $\lambda = \pi \rho_p$. The quantity $P(q)(\epsilon_q^+ - Q_{\perp,q} - Q_{e1,q})$ is the amount of the z^+ cascade power at $\lambda = \pi \rho_p$ that escapes dissipation at $\lambda = \pi \rho_p$ and cascades to $\lambda \ll \rho_p$ as a function of q . Both panels correspond to $r = 2R_\odot$ along the model magnetic-field line that reaches heliolatitude $\Theta = 20.9^\circ$ at large r .

Q_{e1} is spread out more evenly across the δz_p^+ distribution. Figure 6(b) also shows that $Q_{\perp,q} + Q_{e1,q} \simeq \epsilon_q^+$ at $q \leq 7$, which indicates that almost all of the cascade power going into the strongest fluctuations at $\lambda \simeq \rho_p$ is dissipated by stochastic heating and electron LD. Damping at $\lambda \sim \rho_p$ thus truncates the tail of the δz_p^+ distribution, reducing the degree of intermittency at $\lambda \lesssim \rho_p$.

4.5. Energy flux ratios

In figure 7 we plot the individual components of the total energy flux F_{tot} divided by F_{tot} , where F_{tot} is defined in (2.21). To label these components, we have rewritten (2.21) as

$$F_{tot} = F_U + F_g + F_{\text{enth},e} + F_{\text{enth},p} + q_e + q_p + F_w, \quad (4.6)$$

where

$$F_U = \frac{\rho U^3}{2} \quad (4.7)$$

is the bulk-flow kinetic energy flux,

$$F_g = -\frac{GM_\odot \rho U}{r} \quad (4.8)$$

is the gravitational potential-energy flux,

$$F_{\text{enth},e} = \frac{5}{2} n k_B T_e U \quad (4.9)$$

is the electron enthalpy flux,

$$F_{\text{enth},p} = n k_B \left(T_{\perp p} + \frac{3}{2} T_{\parallel p} \right) U \quad (4.10)$$

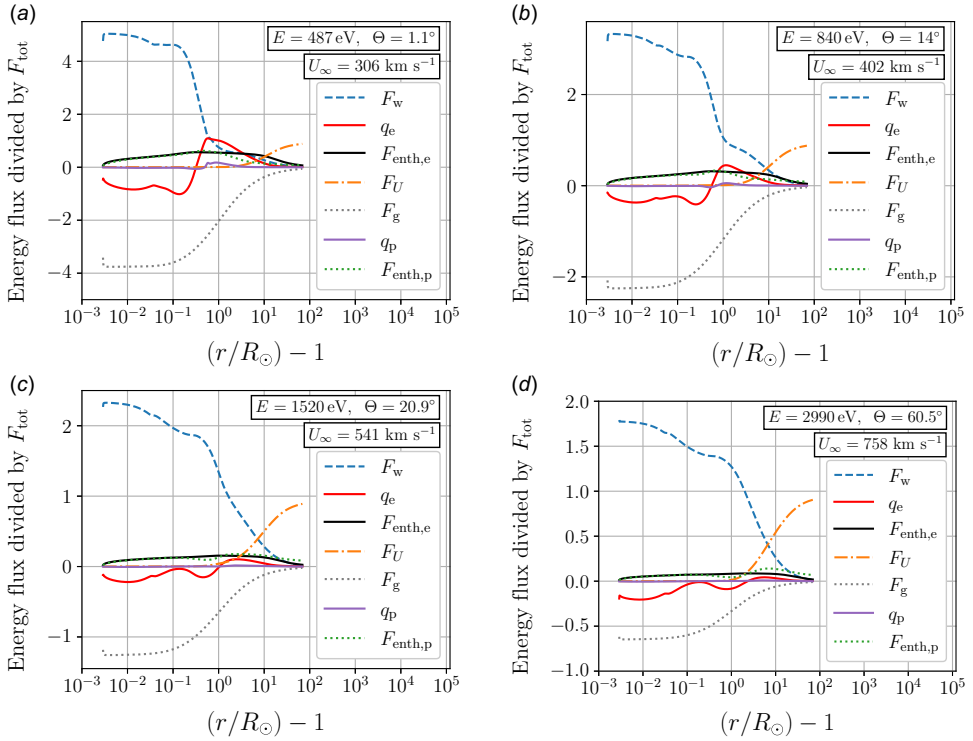


FIGURE 7. The individual energy fluxes defined in (4.7) through (4.12) expressed as fractions of the total energy flux F_{tot} defined in (4.6). Each panel corresponds to a different heliolatitude Θ , asymptotic wind speed U_∞ and energy per proton E .

is the proton enthalpy flux, q_e is the electron heat flux,

$$q_p = q_{\perp p} + q_{\parallel p} \quad (4.11)$$

is the proton heat flux and

$$F_w = \left(\frac{3}{2} U + v_A \right) \mathcal{E}_w \quad (4.12)$$

is the AW enthalpy flux.

As mentioned in § 2.3, outside the low solar corona, radiation can be neglected, and hence, (2.19) implies that

$$a(r) F_{\text{total}}(r) = \text{constant} \quad (4.13)$$

in steady state. As the solar wind flows from the corona out into the distant interplanetary medium, power $a(r) F_{\text{total}}(r)$ is converted from one form to another without loss. At large r , F_{tot} is dominated by F_U , but in the corona F_U is negligible, and thus, F_U/F_{tot} increases with r . Likewise, F_g is large and negative in the corona but negligible at large r , and thus, F_g/F_{tot} increases with r . As $(F_U + F_g)/F_{\text{tot}}$ increases with r , other fractional energy fluxes, such as F_w/F_{tot} , must decrease to maintain total energy conservation, and the fractional energy flux that decreases the most corresponds to the mechanism that is doing the most to accelerate the wind and lift it out of the Sun's gravitational potential well.

Figure 7(a) illustrates a slow-wind stream with asymptotic wind speed $U_\infty = 306 \text{ km s}^{-1}$, where U_∞ is defined in (4.3). This value of U_∞ corresponds to an energy per proton

$$E = \frac{1}{2} m_p U_\infty^2 \quad (4.14)$$

of 487 eV, as indicated in the figure legend. As can be seen in the figure, the primary mechanism that powers the wind is the AW enthalpy flux at $r \lesssim 1.5 R_\odot$, the electron enthalpy flux between $\sim 1.5 R_\odot$ and $\sim 4 R_\odot$, and the electron enthalpy flux at $r \gtrsim 4 R_\odot$.

Figure 7(b,c,d) illustrates wind streams with larger values of U_∞ and E . In these plots the AW enthalpy flux is the dominant driver of the wind out to $r \sim 20\text{--}30 R_\odot$, beyond which some form of enthalpy flux becomes dominant: either a roughly equal mix of $F_{\text{enth,p}}$ and $F_{\text{enth,e}}$ in figure 7(b) or mostly F_p in figures 7(c) and 7(d).

Halekas *et al.* (2023) constructed similar plots using PSP data, but included the electric-potential-energy flux $F_{\Phi_E} = e\Phi_E nU$, which does not appear in our total energy equation. The significance of F_{Φ_E} can be understood by considering single-species versions of the total energy equation, as in equation (23) of Lemaire & Scherer (1973),

$$\begin{aligned} a(r) \left\{ q_e + nU \left[\frac{1}{2} m_e U^2 + k_B \left(\frac{3}{2} T_{\parallel e} + T_{\perp e} \right) + m_e \Phi_g - e\Phi_E \right] \right\} \\ = a(r) F_{\text{tot,e}} = \text{constant}, \end{aligned} \quad (4.15)$$

$$\begin{aligned} a(r) \left\{ q_p + nU \left[\frac{1}{2} m_p U^2 + k_B \left(\frac{3}{2} T_{\parallel p} + T_{\perp p} \right) + m_p \Phi_g + e\Phi_E \right] \right\} \\ = a(r) F_{\text{tot,p}} = \text{constant}, \end{aligned} \quad (4.16)$$

where $T_{\parallel e}$ and $T_{\perp e}$ are the parallel and perpendicular electron temperatures, and $\Phi_g = -GM_\odot/r$ is the gravitational potential. Equations (4.15) and (4.16) do not account for AWs, a point that will come up again following (4.17). When (4.15) and (4.16) are added, the Φ_E terms cancel, which is why Φ_E does not appear in our (4.6) for the total energy flux. Fundamentally, this is because the electric field does no work on a neutral proton–electron plasma, although it does do work on the protons and equal and opposite work on the electrons. Far from the Sun, almost all of the solar-wind energy flux is in the form of the bulk-flow kinetic energy of the protons, which implies that $F_{\text{tot,e}} \ll F_{\text{tot,p}}$ at all r . As the proton bulk-flow kinetic energy flux and gravitational potential-energy flux are at most comparable to $F_{\text{tot,p}}$, the electron bulk-flow kinetic energy flux and gravitational potential-energy flux are everywhere at least a factor of $\simeq m_e/m_p$ smaller than $F_{\text{tot,p}}$, and hence, negligible. After dividing (4.15) by $a(r)$, we are left with three terms that are everywhere $\ll F_{\text{tot,p}}$, namely $F_{\text{tot,e}}$, $nm_e U^3/2$ and $nm_e U \Phi_g$, and three terms that can, at least at some locations, be of the same order of magnitude as $F_{\text{tot,p}}$: q_e , $nUe\Phi_E$ and $5nk_B T_e/2$, where we have set $T_{\parallel e} = T_{\perp e} = T_e$. After dropping the three negligible terms, we can rewrite (4.15) as

$$F_{\Phi_E} \equiv nUe\Phi_E = q_e + \frac{5}{2} nUk_B T_e. \quad (4.17)$$

In other words, the electric-potential-energy flux F_{Φ_E} is approximately the sum of the electron heat flux and electron enthalpy flux. The AW enthalpy flux can lead to violations of (4.17) if the AWs dissipate and heat the electrons. However, we expect (4.17) to be accurate when F_{Φ_E} is large compared with F_w and of the same order of magnitude as $F_{\text{tot,p}}$.

The PSP measurements reported in figure 3 of Halekas *et al.* (2023) show that in the fastest wind streams observed in the study, in which $2000 \text{ eV} < E < 2500 \text{ eV}$, AWs were the dominant energisation mechanism over the comparatively narrow radial interval $13R_{\odot} < r < 23R_{\odot}$. On the other hand, in the slowest wind streams with $E < 500 \text{ eV}$, F_{Φ_E} was the dominant energisation mechanism at $13R_{\odot} < r < 48R_{\odot}$, with q_e significantly smaller than F_{Φ_E} . This latter point implies via (4.17) that F_{enthe} was the dominant energisation mechanism in these low-speed streams at these radii. Taken on their own, these observations are consistent with a long-standing conjecture that the fast solar wind is driven primarily by an AW energy flux, while the slow solar wind is driven by some other mechanism.

However, our results, which provide a model for what is happening interior to the orbit of PSP, paint a different picture. Although the energy flux ratios shown in figure 7 agree with the results from Halekas *et al.* (2023) described in the previous paragraph, in our model F_w is the dominant outward (i.e. positive) energy flux close to the Sun for all values of E . As mentioned previously, for the wind stream modelled in figure 7(a), the dominant energy flux powering the wind is F_w at $r < 1.5R_{\odot}$, q_e between $1.5R_{\odot}$ and $4R_{\odot}$, and F_{enthe} at $r \gtrsim 4R_{\odot}$. Our results show that the observation that F_{enthe} or q_e dominates at large r does not mean that one of these mechanisms dominates near the Sun. Indeed, it would not make sense for F_{enthe} to be the dominant mechanism powering the solar wind between the coronal base and $r \gtrsim 10R_{\odot}$, for if it were then the divergence of the electron enthalpy flux would be large compared with both the turbulent heating rate and the divergence of the electron heat flux. This would cause the electrons to cool approximately adiabatically over this range of radii, which is ruled out by observational constraints on T_e . Nor would it make sense for q_e to be the dominant energy flux powering the solar wind at $r \lesssim 1.5R_{\odot}$, because in this region $\lambda_{\text{mfp}} T_e^{-1} dT_e/dr \ll 1$ and $dT_e/dr > 0$ (see figures 4 and 8), implying that the electron heat flux is well approximated by the Spitzer–Harm formula (2.22) and directed in towards the Sun. In other words, in the low corona, q_e is an energy sink, not an energy source, and therefore, cannot be the dominant energy flux that powers the solar wind. Instead, some non-thermal energy source, such as AWs, is required to power the corona and solar wind (cf. Parker 1965).

Figure 8 provides more detailed information about the solar-wind stream illustrated in figure 7(a), which reaches a heliolatitude of $\Theta = 1.1^\circ$ at large r . As illustrated in figure 2(b), in this wind stream $|B|$ drops rapidly between $r = 1.2R_{\odot}$ and $r = 1.6R_{\odot}$, causing v_A to drop by a factor of almost 10 over this same range of radii, as illustrated in figure 8(b). The resulting large Alfvén-speed gradient leads to strong AW reflection and intense AW dissipation and turbulent heating via (3.19), most of which goes into electron heating because $\delta v_{\text{rms}}/v_A$ is still small enough at these radii (figure 8b) that stochastic ion heating is weaker than electron heating, as shown in figure 8(d). At $1.2R_{\odot} < r \lesssim 2R_{\odot}$, this strong electron heating causes T_e in this slow-wind stream to exceed the value of T_e in the moderately fast solar-wind stream illustrated in figure 4. As the Spitzer–Harm heat flux in (2.22) is $\propto T_e^{7/2}$, the increase in T_e leads to a large increase in q_e , which causes q_e to become the dominant outward energy flux at $1.5R_{\odot} \lesssim r \lesssim 4R_{\odot}$, as shown in figure 7. The reason that the intense heating inside $2R_{\odot}$ decreases U_{∞} relative to the model solution shown in figure 4 is explained following (4.3). Finally, we note that radiative losses are somewhat larger in figure 8(f) than in figure 5(b).

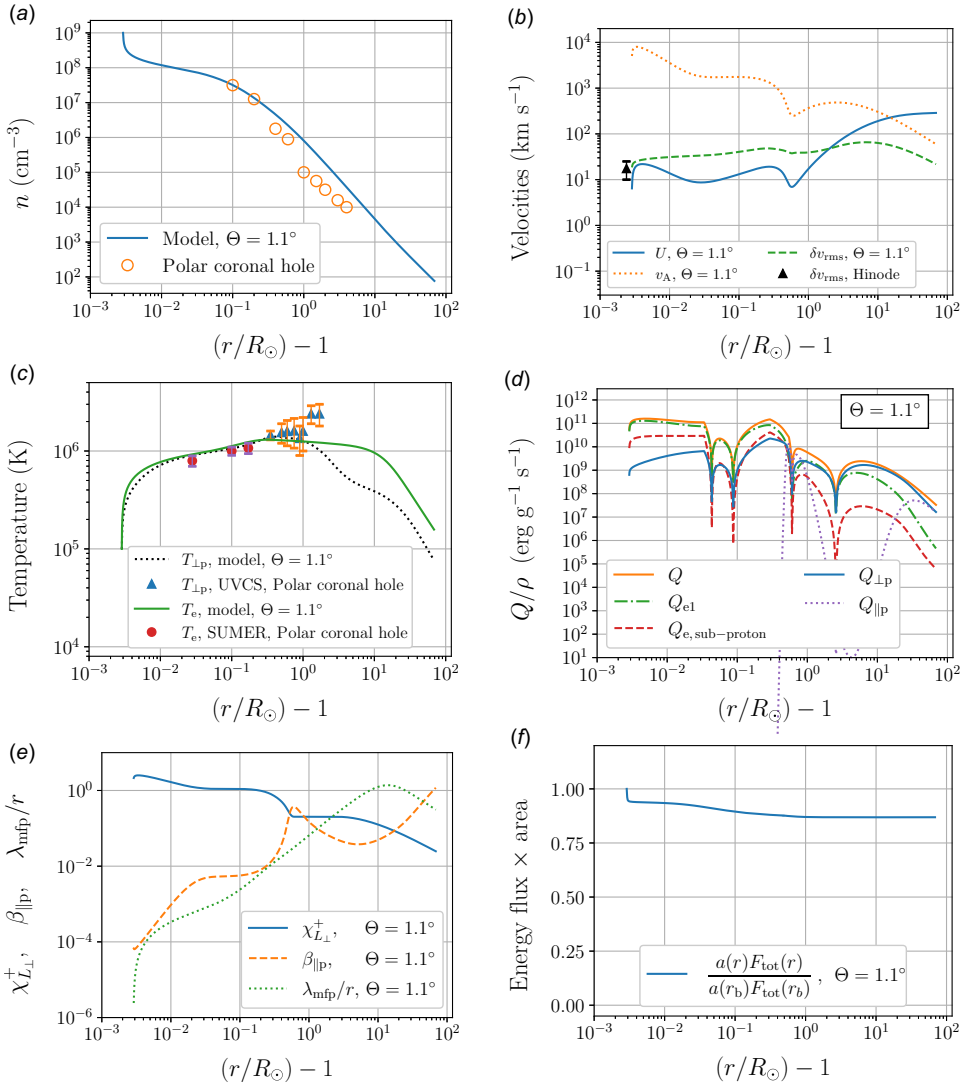


FIGURE 8. Our model solution that reaches heliolatitude $\Theta = 1.1^\circ$ at large r . The various quantities plotted are defined in the captions to figures 4 and 5 and the text following (4.5).

5. Discussion and conclusion

This paper describes a new two-fluid solar-wind model that divides the turbulent heating rate between protons and electrons using a recently developed model of intermittent, reflection-driven Alfvénic turbulence. Intermittency plays an important role in our solar-wind model because it enhances the rate of stochastic ion heating (Mallet *et al.* 2019), which helps to solve the puzzle mentioned in § 1 concerning the origin of the large perpendicular ion temperatures in coronal holes. As shown in § 4, numerical solutions of our model equations agree reasonably well with Ulysses measurements of $U_\infty(\Theta)$, PSP measurements of the radial profiles of n , U , δv_{rms} , $T_{\perp p}$, $T_{\parallel p}$ and T_e , and remote observations of n , δv_{rms} , $T_{\perp p}$ and T_e in coronal holes. We note that explaining the Ulysses measurements of $U_\infty(\Theta)$, and in particular the

latitudinal breadth of the slow wind near solar minimum, has been very challenging for previous AW-driven solar-wind models (cf. Cranmer *et al.* 2007). In part because of this agreement, and in part because the turbulence model that we use (Chandran *et al.* 2025) agrees with PSP observations of solar-wind turbulence near the Sun (Sioulas *et al.* 2024), we believe that our results are a useful step forward in the modelling of turbulent heating in the solar wind. As our treatment of turbulent heating is based entirely on analytic equations, it would be straightforward to incorporate it into other solar-wind models or even models of other astrophysical outflows.

As in the pioneering study by Leer & Holzer (1980), and as discussed in §§ 4.3 and 4.5, the fundamental difference between fast solar wind and slow solar wind in our model lies in the fraction of the AW energy flux that is dissipated close to the Sun. For the axisymmetric solar-minimum magnetic-field model that we adopt in § 4, slow wind arises along the magnetic flux tubes that connect to low heliographic latitudes at large r , and these flux tubes experience very rapid super-radial expansion at $1.2R_{\odot} < r < 1.6R_{\odot}$. This super-radial expansion leads to a large Alfvén-speed gradient in this region, which increases the rate of AW reflection and turbulent heating via (3.19). This rapid heating increases the temperature at $r \lesssim 2R_{\odot}$, which increases the density scale height and loads more mass into the corona out to the sonic critical point, where the plasma becomes gravitationally unbound. The rapid heating at $r \lesssim 2R_{\odot}$ thus increases the mass flux in the solar wind, causing the total energy budget (which is fixed at the coronal base) to be divided up between more particles, leading to a smaller asymptotic wind velocity U_{∞} .

Figure 7 shows that U_{∞} and the proton heating fraction are positively correlated in our model. In particular, the electron enthalpy flux is larger than the proton enthalpy flux at $r = 10R_{\odot}$ in the slowest wind streams, whereas the reverse is true in the fastest wind streams. This correlation is a natural consequence of stochastic heating and the physics of AW propagation in a stratified atmosphere. The stochastic heating rate (3.52) is a strongly increasing function of δv_{rms} , which is, overall, an increasing function of r inside the Alfvén critical point $r_A \sim 10\text{--}20R_{\odot}$ (at which $U = v_A$), as can be seen in figures 4(b) and 8(b). The reason that δv_{rms} increases with r at $r < r_A$ is that, as the AWs propagate away from the Sun into a lower-density plasma, they behave like waves propagating along a tapered string: the AW amplitudes increase, much like a whip cracking. This behaviour is described mathematically by the conservation of AW action, which reduces to conservation of energy when $U \ll v_A$ (see, e.g. Dewar 1970; Heinemann & Olbert 1980).¹⁰ Thus, when the turbulent heating is concentrated close to the Sun, not only is U_{∞} smaller as described in the previous paragraph, but T_p is also smaller because the fluctuation amplitudes are smaller where most of the heating occurs, and electrons therefore receive a larger fraction of the heating rate. Conversely, when the turbulent heating is more extended, the wind is faster and the ions are hotter. Further reinforcing the correlation between T_p and U_{∞} is the fact that strong dissipation of the AW energy flux near the Sun (which reduces U_{∞}) reduces the fluctuation amplitudes farther out in the wind, which decreases the rate of stochastic heating and reduces T_p .

¹⁰In contrast, at $r \gtrsim r_A$, the wave amplitudes decrease with increasing r in part because of the work done by the waves on the moving plasma and in part because of turbulent dissipation.

Although our model is successful in some ways, it has two main weaknesses that should be remedied in future work. First, we use a model of reflection-driven turbulence that assumes that Sunward-propagating Alfvén waves are much weaker than anti-Sunward-propagating Alfvén waves, i.e. $\delta z_{\text{rms}}^- \ll \delta z_{\text{rms}}^+$. However, this assumption becomes inconsistent with the results of this model in the low corona, where $|dv_A/dr|$ is very large. We avoid unphysically large values of $\delta z_{\text{rms}}^-/\delta z_{\text{rms}}^+$ by simply capping $\delta z_{\text{rms}}^-/\delta z_{\text{rms}}^+$ at the value $c_{\text{refl}}(U + v_A)/v_A$, where c_{refl} is a free parameter. However, a more rigorous treatment of wave reflection is needed (see, e.g. Lionello *et al.* 2014a; Shoda, Yokoyama & Suzuki 2018).

The other aspect of our model that needs improvement concerns the turbulent heating rate Q . As described in § 3.5, we account for two contributions to Q : heating from fluctuations at $\lambda \sim \rho_p$, and heating from fluctuations at $\lambda \ll \rho_p$. To compute the heating rate from fluctuations at $\lambda \sim \rho_p$, we first extrapolate the inertial-range scalings of the fluctuation amplitudes all the way to $\lambda \sim \rho_p$, and then we evaluate previously published analytic formulas for the rates at which the fluctuations at $\lambda \sim \rho_p$ lose energy to LD and stochastic heating. We then limit the heating rate at $\lambda \sim \rho_p$ so that it cannot exceed the rate at which δz^+ energy cascades from large scales to small scales through the inertial range (see (3.53) through (3.55)). However, in order for our solar-wind model to match the solar-wind and coronal-hole observations in figures 3 and 4, we must multiply the electron LD rate at $\lambda \sim \rho_p$ by a factor of $c_{\text{LD}} = 0.2$. We conjecture that this is a sign of the helicity barrier, which causes the turbulent power spectrum to steepen at a perpendicular wavenumber k_\perp^* that is smaller than ρ_p^{-1} (Meyrand *et al.* 2021; Squire *et al.* 2022, 2023). Further work, however, is needed to investigate this point and to incorporate the helicity barrier more rigorously into a model of turbulent heating in the solar wind.

Acknowledgements

We thank T. Dennis, M. Kunz, E. Quataert, N. Sioulas, and M. Zhang for valuable discussions.

Editor Thierry Passot thanks the referees for their advice in evaluating this article.

Funding

This work was supported by the National Aeronautics and Space Administration (S.B., grant number NNN06AA01C to the Parker Solar Probe FIELDS Experiment; B.C., grant numbers 80NSSC24K0171, 80NSSC21K1768, and NNN06AA01C; V.D., grant number NNN06AA01C; J.H., grant number NNN06AA01C to the Parker Solar Probe SWEAP Experiment; K.K., grant number NNN06AA01C; R.M., grant number 80NSSC24K0171; J.P., grant number 80NSSC21K1768; E.Y., grant number NNN06AA01C); the U.S. Department of Energy (T.A., contract number DE-AC02-09CH11466); the Japan Society for the Promotion of Science (M.S., KAKENHI Grant Number 24K00688); and the Royal Society Te Apārangi of New Zealand (J.S., Marsden-Fund grant MFP-UOO2221).

Declaration of interests

The authors report no conflict of interest.

REFERENCES

- ALLEN, C.W. 1973 *Astrophysical Quantities*, 3rd edn. University of London, Athlone Press.
- BALE, S.D., *et al.* 2016 The FIELDS instrument suite for solar probe plus. Measuring the coronal plasma and magnetic field, plasma waves and turbulence, and radio signatures of solar transients. *Sp. Sci. Rev.* **204**, 49–82.
- BALE, S.D., KASPER, J.C., HOWES, G.G., QUATAERT, E., SALEM, C. & SUNDKVIST, D. 2009 Magnetic fluctuation power near proton temperature anisotropy instability thresholds in the solar wind. *Phys. Rev. Lett.* **103**, 211101. arXiv: 0908.1274.
- BANASZKIEWICZ, M., AXFORD, W.I. & MCKENZIE, J.F. 1998 An analytic solar magnetic field model. *Astron. Astrophys.* **337**, 940–944.
- BELCHER, J.W. & DAVIS, L., Jr. 1971 Large-amplitude Alfvén waves in the interplanetary medium, 2. *J. Geophys. Res.* **76**, 3534–3563.
- BOE, B., HABBAL, S., DOWNS, C. & DRUCKMÜLLER, M. 2021 The color and brightness of the F-corona inferred from the 2019 July 2 total solar eclipse. *Astrophys. J.* **912**, 44.
- BOE, B., HABBAL, S., DOWNS, C. & DRUCKMÜLLER, M. 2022 The solar minimum eclipse of 2019 July 2. II. The first absolute brightness measurements and MHD model predictions of Fe X, XI, and XIV out to 3.4 R_{\odot} . *Astrophys. J.* **935**, 173.
- BOOK, D.L. 1983 NRL (Naval Research Laboratory) Plasma formulary, revised, Tech. Rep.
- CHANDRAN, B., SIOULAS, N., BALE, S., BOWEN, T., DAVID, V., MEYRAND, R. & YERGER, E. 2025 Intermittent, reflection-driven, strong imbalanced MHD turbulence. *J. Plasm. Phys.* **91**, E57.
- CHANDRAN, B.D.G. 2021 An approximate analytic solution to the coupled problems of coronal heating and solar-wind acceleration. *J. Plasma Phys.* **87**, 905870304.
- CHANDRAN, B.D.G., DENNIS, T.J., QUATAERT, E. & BALE, S.D. 2011 Incorporating kinetic physics into a two-fluid solar-wind model with temperature anisotropy and low-frequency alfvén-wave turbulence. *Astrophys. J.* **743**, 197.
- CHANDRAN, B.D.G. & HOLLWEG, J.V. 2009 Alfvén wave reflection and turbulent heating in the solar wind from 1 solar radius to 1 AU: an analytical treatment. *Astrophys. J.* **707**, 1659–1667.
- CHANDRAN, B.D.G., LI, B., ROGERS, B.N., QUATAERT, E. & GERMASCHESKI, K. 2010 Perpendicular ion heating by low-frequency alfvén-wave turbulence in the solar wind. *Astrophys. J.* **720**, 503–515.
- CHANDRAN, B.D.G. & PEREZ, J.C. 2019 Reflection-driven magnetohydrodynamic turbulence in the solar atmosphere and solar wind. *J. Plasma Phys.* **85**, 905850409.
- CHEN, C.H.K., *et al.* 2020 The evolution and role of solar wind turbulence in the inner heliosphere. *Astrophys. J. Suppl.* **246**, 53.
- CHO, J. & VISHNIAC, E.T. 2000 The anisotropy of magnetohydrodynamic alfvénic turbulence. *Astrophys. J.* **539**, 273–282.
- COLEMAN, P.J. 1968 Turbulence, viscosity, and dissipation in the solar-wind plasma. *Astrophys. J.* **153**, 371.
- CRANMER, S.R. & VAN BALLEGOOIJEN, A.A. 2003 Alfvénic turbulence in the extended solar corona: kinetic effects and proton heating. *Astrophys. J.* **594**, 573–591.
- CRANMER, S.R., VAN BALLEGOOIJEN, A.A. & EDGAR, R.J. 2007 Self-consistent coronal heating and solar wind acceleration from anisotropic magnetohydrodynamic turbulence. *Astrophys. J. Suppl.* **171**, 520–551.
- DAVIS, N., CHANDRAN, B.D.G., BOWEN, T.A., BADMAN, S.T., DE WIT, T.D., CHEN, C.H.K., BALE, S.D., HUANG, Z., SIOULAS, N. & VELLI, M. 2023 The evolution of the 1/f range within a single fast-solar-wind stream between 17.4 and 45.7 solar radii. *Astrophys. J.* **950**, 154.
- DE PONTIEU, B., *et al.* 2007 Chromospheric alfvénic waves strong enough to power the solar wind. *Science* **318**, 1574–1577.
- DEWAR, R.L. 1970 Interaction between hydromagnetic waves and a time-dependent, inhomogeneous medium. *Phys. Fluids* **13**, 2710–2720.
- DMITRUK, P., MATTHAEUS, W.H., MILANO, L.J., OUGHTON, S., ZANK, G.P. & MULLAN, D.J. 2002 Coronal heating distribution due to low-frequency, wave-driven turbulence. *Astrophys. J.* **575**, 571–577.

- DOWNES, C., LIONELLO, R., MIKIĆ, Z., LINKER, J.A. & VELLI, M. 2016 Closed-field coronal heating driven by wave turbulence. *Astrophys. J.* **832**, 180.
- ELSASSER, W.M. 1950 The hydromagnetic equations. *Phys. Rev.* **79**, 183–183.
- ESSER, R., FINESCHI, S., DOBRZYCKA, D., HABBAL, S.R., EDGAR, R.J., RAYMOND, J.C., KOHL, J.L. & GUHATHAKURTA, M. 1999 Plasma properties in coronal holes derived from measurements of minor ion spectral lines and polarized white light intensity. *Astrophys. J. Lett.* **510**, L63–L67.
- GOLDREICH, P. & SRIDHAR, S. 1995 Toward a theory of interstellar turbulence. 2: strong Alfvénic turbulence. *Astrophys. J.* **438**, 763–775.
- GOLDREICH, P. & SRIDHAR, S. 1997 Magnetohydrodynamic turbulence revisited. *Astrophys. J.* **485**, 680–688.
- GOLDSTEIN, B.E., NEUGEBAUER, M., PHILLIPS, J.L., BAME, S., GOSLING, J.T., MCCOMAS, D., WANG, Y.-M., SHEELEY, N.R. & SUESS, S.T. 1996 Ulysses plasma parameters: latitudinal, radial, and temporal variations. *Astron. Astrophys.* **316**, 296–303.
- GOSLING, J.T., ASBRIDGE, J.R., BAME, S.J. & FELDMAN, W.C. 1976 Solar wind speed variations: 1962–1974. *J. Geophys. Res.* **81**, 5061–5070.
- GRAUER, R., KRUG, J. & MARLIANI, C. 1994 Scaling of high-order structure functions in magnetohydrodynamic turbulence. *Phys. Lett. A* **195**, 335–338.
- HACKENBERG, P., MARSCH, E. & MANN, G. 2000 On the origin of the fast solar wind in polar coronal funnels. *Astron. Astrophys.* **360**, 1139–1147.
- HALEKAS, J.S., *et al.* 2023 Quantifying the energy budget in the solar wind from 13.3 to 100 solar radii. *Astrophys. J.* **952**, 2305–13424.
- HANSTEEN, V.H. & VELLI, M. 2012 Solar wind models from the chromosphere to 1 AU. *Sp. Sci. Rev.* **172**, 89–121.
- HEINEMANN, M. & OLBERT, S. 1980 Non-WKB Alfvén waves in the solar wind. *J. Geophys. Res.* **85**, 1311–1327.
- HELLINGER, P., TRÁVNÍČEK, P., KASPER, J.C. & LAZARUS, A.J. 2006 Solar wind proton temperature anisotropy: linear theory and WIND/SWE observations. *Geophys. Res. Lett.* **33**, 9101.
- HOLLWEG, J.V. 1974 On electron heat conduction in the solar wind. *J. Geophys. Res.* **79**, 3845–3850.
- HOLLWEG, J.V. 1976 Collisionless electron heat conduction in the solar wind. *J. Geophys. Res.* **81**, 1649–1658.
- HOLLWEG, J.V., CRANMER, S.R. & CHANDRAN, B.D.G. 2010 Coronal Faraday rotation fluctuations and a wave/turbulence-driven model of the solar wind. *Astrophys. J.* **722**, 1495–1503.
- HOLLWEG, J.V. & ISENBERG, P.A. 2002 Generation of the fast solar wind: a review with emphasis on the resonant cyclotron interaction. *J. Geophys. Res. (Sp. Phys.)* **107**, 1147.
- HOWES, G.G. 2024 The fundamental parameters of astrophysical plasma turbulence and its dissipation: non-relativistic limit. *J. Plasma Phys.* **90**, 905900504.
- HOWES, G.G., COWLEY, S.C., DORLAND, W., HAMMETT, G.W., QUATAERT, E. & SCHEKOCHIHIN, A.A. 2006 Astrophysical gyrokinetics: basic equations and linear theory. *Astrophys. J.* **651**, 590–614.
- HU, Y.Q., ESSER, R. & HABBAL, S.R. 2000 A four-fluid turbulence-driven solar wind model for preferential acceleration and heating of heavy ions. *J. Geophys. Res.* **105**, 5093–5112.
- HUANG, Z., *et al.* 2023 New observations of solar wind 1/f turbulence spectrum from Parker Solar Probe. *Astrophys. J. Lett.* **950**, L8.
- KASPER, J.C., *et al.* 2016 Solar wind electrons alphas and protons (SWEAP) investigation: design of the solar wind and coronal plasma Instrument suite for Solar Probe Plus. *Sp. Sci. Rev.* **204**, 131–186.
- KASPER, J.C., LAZARUS, A.J. & GARY, S.P. 2002 Wind/SWE observations of firehose constraint on solar wind proton temperature anisotropy. *Geophys. Res. Lett.* **29**, 170000–170001.
- KOHL, J.L., *et al.* 1998 UVCS/SOHO empirical determinations of anisotropic velocity distributions in the solar corona. *Astrophys. J. Lett.* **501**, L127–L131.
- KOPP, R.A. & HOLZER, T.E. 1976 Dynamics of coronal hole regions. I - steady polytropic flows with multiple critical points. *Sol. Phys.* **49**, 43–56.
- KRAICHNAN, R.H. 1965 Inertial-range spectrum of hydromagnetic turbulence. *Phys. Fluids* **8**, 1385–1387.
- KULSRUD, R. 1983 In *Handbook of Plasma Physics* (ed. Rosenbluth M.N. & Sagdeev R.Z.), pp. 115. North Holland.

- LANDI, E. 2008 The off-disk thermal structure of a polar coronal hole. *Astrophys. J.* **685**, 1270–1276.
- LEAMON, R.J., MATTHAEUS, W.H., SMITH, C.W. & WONG, H.K. 1998 Contribution of cyclotron-resonant damping to kinetic dissipation of interplanetary turbulence. *Astrophys. J. Lett.* **507**, L181–L184.
- LEER, E. & HOLZER, T.E. 1980 Energy addition in the solar wind. *J. Geophys. Res.* **85**, 4681–4688.
- LEMAIRE, J. & SCHERER, M. 1973 Kinetic models of the solar and polar winds. *Rev. Geophys. Sp. Ge.* **11**, 427–468.
- LIONELLO, R., VELLI, M., DOWNS, C., LINKER, J.A. & MIKIĆ, Z. 2014a Application of a solar wind model driven by turbulence dissipation to a 2D magnetic field configuration. *Astrophys. J.* **796**, 111.
- LIONELLO, R., VELLI, M., DOWNS, C., LINKER, J.A., MIKIĆ, Z. & VERDINI, A. 2014b Validating a time-dependent turbulence-driven model of the solar wind. *Astrophys. J.* **784**, 120.
- LITHWICK, Y., GOLDREICH, P. & SRIDHAR, S. 2007 Imbalanced strong MHD turbulence. *Astrophys. J.* **655**, 269–274.
- LIVI, R., *et al.* 2022 The solar probe ANalyzer-ions on the parker solar probe. *Astrophys. J.* **938**, 138.
- MALLET, A., KLEIN, K.G., CHAND, RAN, HOPPOCK, I.W., BOWEN, T.A., SALEM, C.S. & BALE, S.D. 2019 Interplay between intermittency and dissipation in collisionless plasma turbulence. *J. Plasma Phys.* **85**, 175850302.
- MALLET, A. & SCHEKOCHIHIN, A.A. 2017 A statistical model of three-dimensional anisotropy and intermittency in strong alfvénic turbulence. *Mon. Not. R. Astron. Soc.* **466**, 3918–3927.
- MALLET, A., SCHEKOCHIHIN, A.A. & CHANDRAN, B.D.G. 2015 Refined critical balance in strong alfvénic turbulence. *Mon. Not. R. Astron. Soc.* **449**, L77–L81.
- MCCHESENEY, J.M., STERN, R.A. & BELLAN, P.M. 1987 Observation of fast stochastic ion heating by drift waves. *Phys. Rev. Lett.* **59**, 1436–1439.
- MCCOMAS, D.J., BARRACLOUGH, B.L., FUNSTEN, H.O., GOSLING, J.T., SANTIAGO-MUÑOZ, E., SKOUG, R.M., GOLDSTEIN, B.E., NEUGEBAUER, M., RILEY, P. & BALOGH, A. 2000 Solar wind observations over Ulysses' first full polar orbit. *J. Geophys. Res.* **105**, 10419–10434.
- MCCOMAS, D.J., ELLIOTT, H.A., SCHWADRON, N.A., GOSLING, J.T., SKOUG, R.M. & GOLDSTEIN, B.E. 2003 The three-dimensional solar wind around solar maximum. *Geophys. Res. Lett.* **30**, 1517.
- MCINTYRE, J.R., CHEN, C.H.K., SQUIRE, J., MEYRAND, R. & SIMON, P.A. 2024 Evidence for the helicity barrier from measurements of the turbulence transition range in the solar wind. arXiv:2407.10815.
- MEYRAND, R., SQUIRE, J., MALLET, A. & CHANDRAN, B.D.G. 2025 Reflection-driven turbulence in the super-alfvénic solar wind. *J. Plasma Phys.* **91**, E29.
- MEYRAND, R., SQUIRE, J., SCHEKOCHIHIN, A.A. & DORLAND, W. 2021 On the violation of the zeroth law of turbulence in space plasmas. *J. Plasma Phys.* **87**, 535870301.
- MIKIĆ, Z., *et al.* 2018 Predicting the corona for the 21 August 2017 total solar eclipse. *Nat. Astron.* **2**, 913–921.
- MONCUQUET, M., *et al.* 2020 First in situ measurements of electron density and temperature from quasi-thermal noise spectroscopy with parker solar probe/FIELDS. *Astrophys. J.* **246**, 44.
- NEUGEBAUER, M. & SNYDER, C.W. 1966 Mariner 2 observations of the solar wind, 1, average properties. *J. Geophys. Res.* **71**, 4469–4484.
- NG, C.S. & BHATTACHARJEE, A. 1996 Interaction of shear-alfven wave packets: implication for weak magnetohydrodynamic turbulence in astrophysical plasmas. *Astrophys. J.* **465**, 845.
- NG, C.S. & BHATTACHARJEE, A. 1997 Scaling of anisotropic spectra due to the weak interaction of shear-Alfvén wave packets. *Phys. Plasmas* **4**, 605–610.
- PARKER, E.N. 1965 Dynamical theory of the solar wind. *Sp. Sci. Rev.* **4**, 666.
- PEREZ, J.C. & CHANDRAN, B.D.G. 2013 Direct numerical simulations of reflection-driven, reduced MHD turbulence from the sun to the alfvén critical point. *Astrophys. J.* **776**, 124.
- POLITANO, H. & POUQUET, A. 1995 Model of intermittency in magnetohydrodynamic turbulence. *Phys. Rev. E.* **52**, 636–641.
- QUATAERT, E. 1998 Particle heating by Alfvénic turbulence in hot accretion flows. *Astrophys. J.* **500**, 978–991.
- RAOUAFI, N.E., *et al.* 2023 Parker Solar Probe: Four Years of Discoveries at Solar Cycle Minimum. *Sp. Sci. Rev.* **219**, 8.

- RAPPAZZO, A.F., MATTHAEUS, W.H., RUFFOLO, D., VELLI, M. & SERVIDIO, S. 2017 Coronal heating topology: the interplay of current sheets and magnetic field lines. *Astrophys. J.* **844**, 87.
- RAPPAZZO, A.F., VELLI, M., EINAUDI, G. & DAHLBURG, R.B. 2007 Coronal heating, weak MHD turbulence, and scaling laws. *Astrophys. J. Lett.* **657**, L47–L51.
- RÉVILLE, V., *et al.* 2020 The role of Alfvén wave dynamics on the large-scale properties of the solar wind: comparing an MHD simulation with Parker solar probe E1 data. *Astrophys. J. Suppl.* **246**, 24.
- RIVERA, Y.J., *et al.* 2024 In situ observations of large-amplitude Alfvén waves heating and accelerating the solar wind. *Science* **385**, 962–966.
- SCHUNK, R.W. 1975 Transport equations for aeronomy. *Planet. Space Sci.* **23**, 437–485.
- SHARMA, P., HAMMETT, G.W., QUATAERT, E. & STONE, J.M. 2006 Shearing box simulations of the MRI in a collisionless plasma. *Astrophys. J.* **637**, 952–967.
- SHEBALIN, J.V., MATTHAEUS, W. & MONTGOMERY, D. 1983 Anisotropy in MHD turbulence due to a mean magnetic field. *J. Plasma Phys.* **29**, 525–547.
- SHODA, M., SUZUKI, T.K., ASGARI-TARGHI, M. & YOKOYAMA, T. 2019 Three-dimensional simulation of the fast solar wind driven by compressible magnetohydrodynamic turbulence. *Astrophys. J.* **880**, L2.
- SHODA, M., YOKOYAMA, T. & SUZUKI, T.K. 2018 A self-consistent model of the coronal heating and solar wind acceleration including compressible and incompressible heating processes. *Astrophys. J.* **853**, 190.
- SIOULAS, N., *et al.* 2024 Higher-order analysis of three-dimensional anisotropy in imbalanced alfvénic turbulence. [arXiv:2404.04055](https://arxiv.org/abs/2404.04055).
- SNYDER, P.B., HAMMETT, G.W. & DORLAND, W. 1997 Landau fluid models of collisionless magnetohydrodynamics. *Phys. Plasmas* **4**, 3974–3985.
- SPITZER, L. & HÄRM, R. 1953 Transport phenomena in a completely ionized gas. *Phys. Rev.* **89**, 977–981.
- SQUIRE, J., MEYRAND, R. & KUNZ, M.W. 2023 Electron-ion heating partition in imbalanced solar-wind turbulence. *Astrophys. J. Lett.* **957**, L30.
- SQUIRE, J., MEYRAND, R., KUNZ, M.W., ARZAMASSKIY, L., SCHEKOCIHIN, A.A. & QUATAERT, E. 2022 High-frequency heating of the solar wind triggered by low-frequency turbulence. *Nat. Astron.* **6**, 715–723.
- SUZUKI, T.K. 2006 Forecasting solar wind speeds. *Astrophys. J. Lett.* **640**, L75–L78.
- SUZUKI, T.K. & INUTSUKA, S.-I. 2005 Making the corona and the fast solar wind: a self-consistent simulation for the low-frequency alfvén waves from the photosphere to 0.3 AU. *Astrophys. J. Lett.* **632**, L49–L52.
- USMANOV, A.V., GOLDSTEIN, M.L. & MATTHAEUS, W.H. 2014 Three-fluid, three-dimensional magnetohydrodynamic solar wind model with eddy viscosity and turbulent resistivity. *Astrophys. J.* **788**, 43.
- VAN BALLEGOOIJEN, A.A. & ASGARI-TARGHI, M. 2016 Heating and acceleration of the fast solar wind by alfvén wave turbulence. *Astrophys. J.* **821**, 106.
- VAN DER HOLST, B., SOKOLOV, I.V., MENG, X., JIN, M., MANCHESTER, W.B., IV, TÓTH, G. & GOMBOSI, T.I. 2014 Alfvén wave solar model (AWSOM): coronal heating. *Astrophys. J.* **782**, 81.
- VELLI, M. 1993 On the propagation of ideal, linear Alfvén waves in radially stratified stellar atmospheres and winds. *Astron. Astrophys.* **270**, 304–314.
- VELLI, M., GRAPPIN, R. & MANGENEY, A. 1989 Turbulent cascade of incompressible unidirectional Alfvén waves in the interplanetary medium. *Phys. Rev. Lett.* **63**, 1807–1810.
- VERDINI, A. & VELLI, M. 2007 Alfvén waves and turbulence in the solar atmosphere and solar wind. *Astrophys. J.* **662**, 669–676.
- VERDINI, A., VELLI, M., MATTHAEUS, W.H., OUGHTON, S. & DMITRUK, P. 2010 A turbulence-driven model for heating and acceleration of the fast wind in coronal holes. *Astrophys. J. Lett.* **708**, L116–L120.
- VERSCHAREN, D., CHANDRAN, B.D.G., JEONG, S.-Y., SALEM, C.S., PULUPA, M.P. & BALE, S.D. 2019 Self-induced scattering of strahl electrons in the solar wind. *Astrophys. J.* **886**, 136.
- WHITTLESEY, P.L., *et al.* 2020, The solar probe analyzers – electrons on the Parker solar probe, *Astrophys. J. Suppl. Ser.* **246**, 74.